

Whole rock basalt alteration from CO₂-rich brine during flow-through experiments at 150°C and 150 bar

Andrew J. Luhmann^{*1,2}, Benjamin M. Tutolo^{2,3}, Chunyang Tan², Bruce M. Moskowitz^{2,4}, Martin O. Saar^{2,5}, William E. Seyfried, Jr.²

¹Department of Earth and Environmental Science, New Mexico Institute of Mining and Technology, 801 Leroy Place, Socorro, NM 87801, USA

²Department of Earth Sciences, University of Minnesota, 310 Pillsbury Drive SE, Minneapolis, MN 55455, USA

³Department of Earth Sciences, University of Oxford, South Parks Road, Oxford, OX1 3AN, UK.

⁴Institute for Rock Magnetism, University of Minnesota, 100 Union Street SE, Minneapolis, MN 55455, USA

⁵Geothermal Energy and Geofluids Group, Department of Earth Sciences, ETH-Zürich, 8092 Zürich, Switzerland

*Corresponding author. Department of Earth and Environmental Science, New Mexico Institute of Mining and Technology, 801 Leroy Place, Socorro, NM 87801, USA. Tel: 1-575-835-5029; fax: 1-575-835-6436. Email address: ajl@nmt.edu (A.J. Luhmann).

Abstract

Four flow-through experiments at 150°C were conducted on intact cores of basalt to assess alteration and mass transfer during reaction with CO₂-rich fluid. Two experiments used a flow rate of 0.1 ml/min, and two used a flow rate of 0.01 ml/min. Permeability increased for both experiments at the higher flow rate, but decreased for the lower flow rate experiments. The

experimental fluid (initial pH of 3.3) became enriched in Si, Mg, and Fe upon passing through the cores, primarily from olivine and titanomagnetite dissolution and possibly pyroxene dissolution. Secondary minerals enriched in Al and Si were present on post-experimental cores, and an Fe₂O₃-rich phase was identified on the downstream ends of the cores from the experiments at the lower flow rate. While we could not specifically identify if siderite (FeCO₃) was present in the post-experimental basalt cores, siderite was generally saturated or supersaturated in outlet fluid samples, suggesting a thermodynamic drive for Fe carbonation from basalt-H₂O-CO₂ reaction. Reaction path models that employ dissolution kinetics of olivine, labradorite, and enstatite also suggest siderite formation at low pH. Furthermore, fluid-rock interaction caused a relatively high mobility of the alkali metals; up to 27% and 100% of the K and Cs present in the core, respectively, were preferentially dissolved from the cores, likely due to fractional crystallization effects that made alkali metals highly accessible. Together, these datasets illustrate changes in chemical parameters that arise due to fluid-basalt interaction in relatively low pH environments with elevated CO₂.

Keywords: basalt alteration, carbon sequestration, fluid-rock reaction, olivine dissolution, permeability, reactive transport

1. Introduction

Basalt is the most common rock at the Earth's surface, covering much of the ocean floor (Goldberg and Slagle, 2009) as well as significant portions of the continents (Dessert et al., 2003; McGrail et al., 2006; Oelkers et al., 2008; Snæbjörnsdóttir et al., 2014). Reaction between CO₂ and basalt in the ocean crust plays an important role in the regulation of atmospheric CO₂

(Coogan and Gillis, 2013). CO₂ is also present in higher concentrations in the natural environment (Federico et al., 2002, 2004; Flaathen et al., 2009; Fridriksson et al., 2006; Kerrick, 2001; Lupton et al., 2006; Mörner and Etiope, 2002; Watson et al., 2004), and can lead to significant basalt-CO₂-rich fluid interaction (Rogers et al., 2006). CO₂ increases the acidity of groundwater, which ultimately increases groundwater metal concentrations due to reaction of unstable minerals in rocks (Aiuppa et al., 2000). Accordingly, CO₂-rich fluid-basalt reaction can lead to conversion of CO₂ to carbonate minerals (Flaathen et al., 2009; Rogers et al., 2006). Furthermore, toxic metals liberated by dissolution are generally incorporated into secondary mineral phases (Flaathen et al., 2009; Olsson et al., 2014; Wigley et al., 2013). It is for all of these reasons that basalt has been proposed as an ideal injection formation for carbon capture and geologic sequestration (CCS) operations to reduce anthropogenic CO₂ emissions (IPCC, 2005; NACSA, 2012); namely, dissolution of olivine, pyroxene, and plagioclase by CO₂-charged fluids will produce abundant cations in solution that will ultimately be available for carbonate formation (e.g., Gislason and Oelkers, 2014; Goldberg et al., 2008; Matter and Kelemen, 2009; Matter et al. 2016; McGrail et al., 2006; Oelkers et al., 2008).

Dissolution rates of olivine, pyroxene, and plagioclase have been reported in many previous studies. Rates of olivine dissolution generally increase with increasing temperature and decrease with increasing pH (e.g., Chen and Brantley, 2000; Hänchen et al., 2006; Pokrovsky and Schott, 2000; Rosso and Rimstidt, 2000; Wogelius and Walther, 1991). Pyroxene dissolution rates also increase with increasing temperature and decrease with increasing pH (Chen and Brantley, 1998; Knauss et al., 1993; Oelkers and Schott, 2001), although pyroxene dissolution rates are slower than olivine dissolution rates. Dissolution rates of plagioclase portray a characteristic U-shaped curve as a function of pH, where rates are lowest at

intermediate pH and increase as pH becomes more acidic or alkaline (Chou and Wollast, 1985; Gudbrandsson et al., 2014; Knauss and Wolery, 1986). A similar U-shaped curve also characterizes basaltic glass dissolution rates as a function of pH (Gislason and Oelkers, 2003; Guy and Schott, 1989).

A number of studies have considered various scenarios of CO₂-H₂O-basalt/olivine/basaltic glass interaction to quantify rates of reaction and document alteration phases, with a particular focus on carbonation (Daval et al., 2011; Felmy et al., 2012; Galeczka et al., 2014; Giammar et al., 2005; Gysi and Stefánsson, 2012a, 2012b, 2012c; Johnson et al., 2014; Matter et al., 2007; McGrail et al., 2006; Rosenbauer et al., 2012; Schaef et al., 2010, 2011, 2012, 2013, 2014; Schaef and McGrail, 2009). Andreani et al. (2009) and Peuble et al. (2015) conducted reactive percolation experiments on sintered dunite and sintered olivine cores, respectively, where they flowed CO₂-rich fluid with significant dissolved NaHCO₃ (pH = 6.6 to 6.7) through the cores. These studies demonstrated the importance of flow rate in controlling degree of carbonation and permeability changes, and Peuble et al. (2015) noted that carbonation rates from their experiments representing a rock-dominated system are much lower than previously published values from water-dominated experimental setups. Field projects are currently underway to explore the feasibility of sequestering CO₂ as carbonates in basaltic reservoirs in southwest Iceland (Gislason et al., 2010; Matter et al., 2009, 2011) and in the northwest United States in Washington (McGrail et al., 2011). Recent research at the CarbFix site in Iceland found that more than 95% of the injected CO₂ was converted into carbonate minerals within two years (Matter et al. 2016).

In this study, we report on four experiments where CO₂-charged brine flowed through intact basalt cores. We use a low pH experimental fluid (initial pH of 3.3) to provide a strong

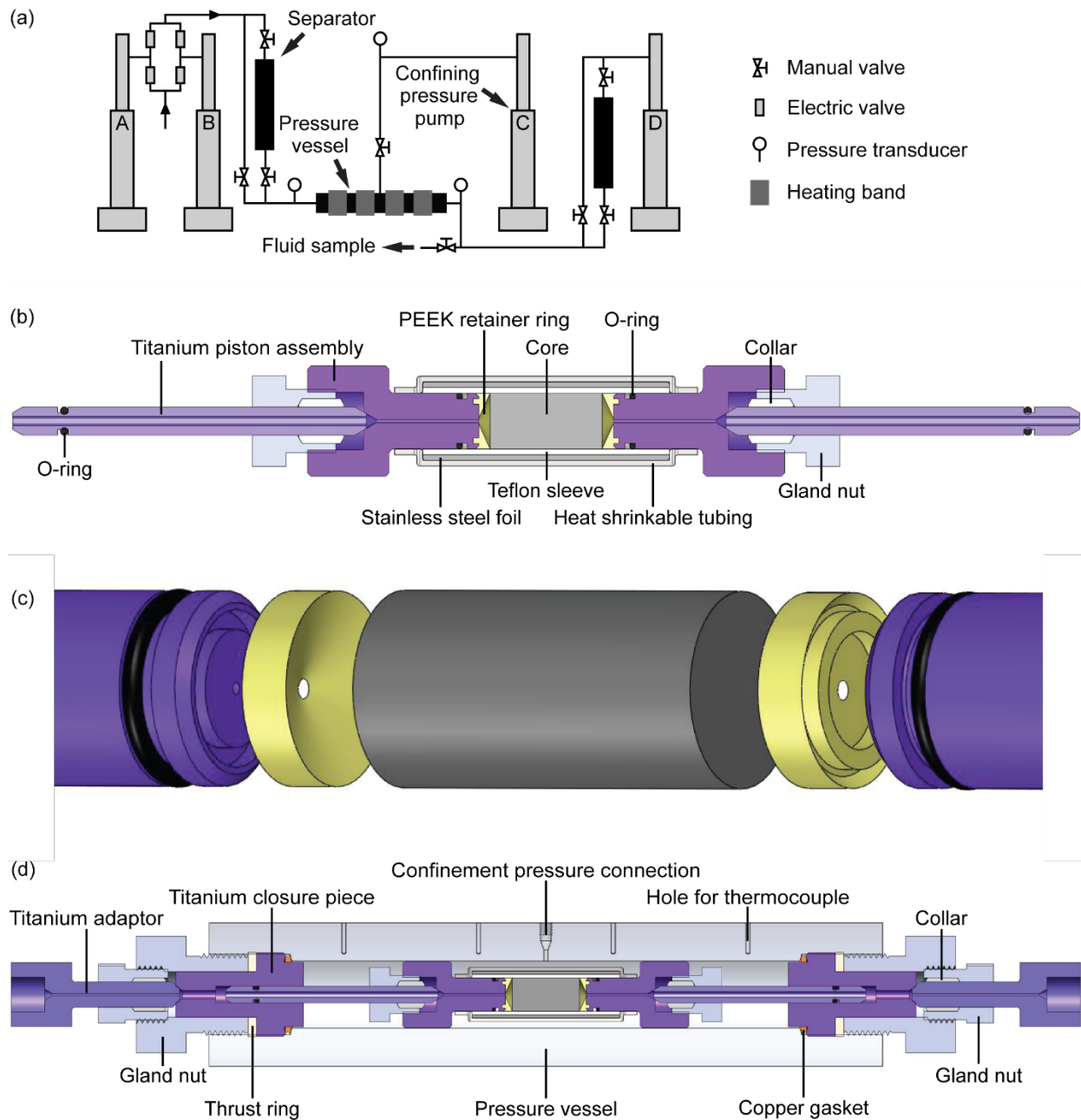
drive for reaction to determine the extent of cation liberation that would ultimately be available for carbonation. The experiments were conducted to better understand basalt alteration due to reaction with CO₂-rich brine and to explore feedbacks between chemical reactions and permeability changes in CO₂-rich reservoirs. We also run simulations of fluid-basalt reaction to assess mass transfer and alteration over longer reaction timescales. While this paper focuses on chemical aspects of basalt alteration, a companion paper focuses on physical property changes (porosity, permeability, and surface area) arising from the experiments (Luhmann et al., in review). In the complementary paper, we use X-ray computed tomography (XRCT) and small-angle (SANS) and ultra-small-angle neutron scattering (USANS) to characterize changes in porosity and surface area at a range of scales. Ultimately, the coupling of various datasets facilitates a more complete understanding of the physical and chemical evolution of fluid and rock during the interaction of basalt and CO₂-rich fluid.

2. Methods

Experiments were conducted using a hydrothermal flow system reactor employed in previous carbon sequestration experiments (Luhmann et al., 2013, 2014; Tutolo et al., 2014, 2015). The flow system uses Teledyne ISCO syringe pumps, an Autoclave Engineers stainless steel pressure vessel, Watlow band heaters, Heise pressure transducers, titanium separators, and other components to conduct experiments at elevated temperature and pressure while continuously measuring permeability (Figure 1a). Darcy's law facilitates calculation of permeability, k (Darcy, 1856):

$$k = -\frac{Q_v \mu L}{A_c \Delta P}, \quad (1)$$

115 where Q_v is the volumetric fluid flow rate, μ is the fluid dynamic viscosity, L is the core sample
 116 length, A_c is the cross-sectional area of the core, and ΔP is the pressure change over the core
 117 length. The dynamic viscosity of a 1 molal NaCl solution at 150°C and 150 bar is 212.2 $\mu\text{Pa s}$
 118 (Kestin et al., 1981; Mao and Duan, 2009). Fluid samples are also periodically collected via a
 119 Hoke valve to gauge fluid-rock interaction.



120

Figure 1. (a) Flow system used for experiments of basalt alteration. (b) Ti piston assemblies with rock core and other components that facilitate flow of experimental solution through the core sample. (c) A PEEK retainer ring is placed just upstream and downstream of the core sample. One side snaps into the Ti piston assembly, and the cone on the other side facilitates inflow and outflow of experimental fluid to and from all potential flow paths in the core. (d) Flow-through reaction cell that incorporates a modified pressure vessel and many custom-made components. While the confinement fluid (DI H₂O) is in contact with the stainless steel pressure vessel and other stainless steel components, flowing experimental fluid only contacts corrosion-resistant Ti, PEEK, and Teflon components while heated to experimental temperatures within or near the pressure vessel. Kalrez O-rings on piston assemblies facilitate axial pressure on the core, so confining fluid provides both axial and radial pressure on the core. Purple colors in (b)-(d) indicate Ti components.

An experimental core is loaded into a flow-through reaction cell that includes both readily available and custom-made components (Figure 1b-d). Cores are contained within a 1.3 cm inner diameter Teflon FEP sheath with a 0.08 cm wall thickness, and the Teflon is wrapped in 0.005 cm stainless steel foil to limit CO₂ diffusion into the confining fluid (Figure 1b). The foil is held in place by PVDF heat-shrinkable tubing. We make use of titanium (Ti-6Al-4V) piston assemblies upstream and downstream of the core to couple the Teflon-sheathed core to the flow system. Each Ti assembly consists of two pieces connected using a standard high pressure cone seal that employs a Heli-Coil insert (stainless steel threads to prevent deformation of Ti). Kalrez O-rings (compound 3018, size 006 and 012) are placed at both ends of the Ti piston assemblies that link the inflow and outflow pressure lines to the Teflon-sheathed rock core. A

novel design of the reaction cell is the use of O-rings on the Ti piston assemblies within the pressure vessel. Confinement fluid pressure is always set higher than pore-fluid pressure, and because the confinement fluid surrounds the core and the piston assemblies between the two small O-rings at the end of the pistons, the higher confining pressure moves the pistons inward to compress the core in an axial orientation. Furthermore, the Teflon transfers the confining pressure to the core in a radial orientation, ensuring that flow occurs through the core sample. Thus, confining pressure is applied in all directions to the experimental core. PEEK retainer rings are placed between the core and the piston assemblies (Figure 1c). One side of each retainer ring snaps into its respective Ti piston assembly. A cone is cut on the core side of the ring, ensuring that the reactant fluid effectively penetrates all potential flow paths in the rock core. PEEK retainer rings are sufficiently flexible to preclude damaging the integrity of the rock core, yet strong enough to maintain shape with minimal deformation.

The core, Ti piston assemblies, and retainer rings are installed within a stainless steel pressure vessel (Figure 1d). We have employed an Autoclave Engineers keuntzel closure, double ended, stainless steel pressure vessel (model number KD10.3SS11). The double ended design enables installation of components internal to the vessel. We have modified the vessel by drilling a hole through the center and adding a cone seal, which enables connection to a pump to provide fluid confinement pressure via 1/16 in stainless steel tubing. Furthermore, thermocouples are inserted into holes 1.1 cm deep and 1.7 mm wide that were drilled into the vessel to monitor temperature of the reaction cell. The pressure vessel includes standard stainless steel closure pieces. One end of each Ti piston assembly is inserted into one of the closure pieces. Because we have observed reaction between experimental fluid and stainless steel at 150°C (Tutolo et al., 2015), we replaced the stainless steel closures provided with the

Autoclave Engineers pressure vessel with functionally similar devices, but made of titanium to prevent corrosion of this component of the reaction cell. We also designed Ti adaptors that are external to the pressure vessel and form a cone seal with each closure piece so that all flow components that are heated and in contact with experimental fluids are made of corrosion-resistant materials. Furthermore, all Ti components, both internal and external to the pressure vessel, were heated to 500°C in air to enhance formation of a thin TiO₂ coating that further inhibits corrosion, especially by oxidizing and acidic NaCl fluids. Finally, we use a copper gasket to form the metal to metal seal between each Ti closure piece and the seat of the stainless steel pressure vessel.

Basalt used in experiments was from the Eastern Snake River Plain, Idaho. Cores were cut from the 243 ft borehole interval of borehole Test Area North (TAN) 33 (43.84739°N, 112.70444°W), which was drilled at the site of the Idaho National Lab. Physical and chemical properties of basalt from this site have been documented in several publications (e.g., Ackerman, 1991; McLing, 1994; Hughes et al., 2002). Intact cores permitted experimental fluid to flow through natural pathways, which were then modified due to fluid-rock interaction with reaction progress. Tables 1 and 2 provide the major oxide and trace element compositions, respectively, of the basalt. Following digestion, major oxides were analyzed with an inductively coupled plasma-optical emission spectrometer (ICP-OES, 2σ accuracies of 3%), and trace elements were analyzed with an inductively coupled plasma-mass spectrometer (ICP-MS, 2σ accuracies of 5%). Normalized mineralogy of major oxide data indicates the following mineral composition: 48.5 wt% plagioclase, 13.8 wt% olivine, 12.5 wt% diopside, 12.4 wt% hypersthene, 5.43 wt% ilmenite, 4.71 wt% orthoclase, 1.74 wt% apatite, 1.13 wt% magnetite, and 0.09 wt% zircon¹. An

¹ Calculated using Kurt Hollocher's CIPW Norm Excel program (http://minerva.union.edu/hollochk/c_petrology/norms.htm).

energy dispersive X-ray spectroscopy (EDS) spot analysis on an olivine crystal (shown in Figure 6a) revealed an olivine composition of Fo70. Samples were fully crystalline, as thin section microscopy did not reveal any basaltic glass (Figure 2). Given the crystal size and lack of glass, the basalt would be better characterized as diabase, but we refer to basalt for simplicity. An ultrasonic bath was used to remove loose, fine particles from the cores that were generated while cutting, and an oven at 60°C was used to dry cores pre- and post-experiment to determine mass changes from experimental basalt alteration.

Table 1
Major oxide composition of basalt.

Oxide	wt%
Al ₂ O ₃	14.8
BaO	0.050
CaO	9.2
FeO	14.0
K ₂ O	0.76
MgO	7.1
MnO	0.206
Na ₂ O	2.65
P ₂ O ₅	0.75
SiO ₂	48
SrO	0.040
TiO ₂	2.86
ZrO ₂	0.042
Total	100

Table 2
Trace element composition of basalt.

Trace element	ppm
Li	7.4
Sc	28
V	300
Cr	219
Ni	77
Cu	40
Zn	180
Ga	24
As	1.7 ^a

Rb	12.5
Sr	360
Y	41
Zr	330
Nb	37
Mo	2.6
Sn	1.7
Cs	0.30
Ba	530
La	41
Ce	88
Pr	10.8
Nd	46
Sm	9.6
Eu	3.1
Gd	9.8
Tb	1.40
Dy	8.4
Ho	1.62
Er	4.5
Tm	0.62
Yb	3.9
Lu	0.56
Hf	6.9
Ta	4.3
Pb	7.0
Th	1.7
U	0.54

^aAnalyzed value is not larger than 2× the 2σ error.

200
201

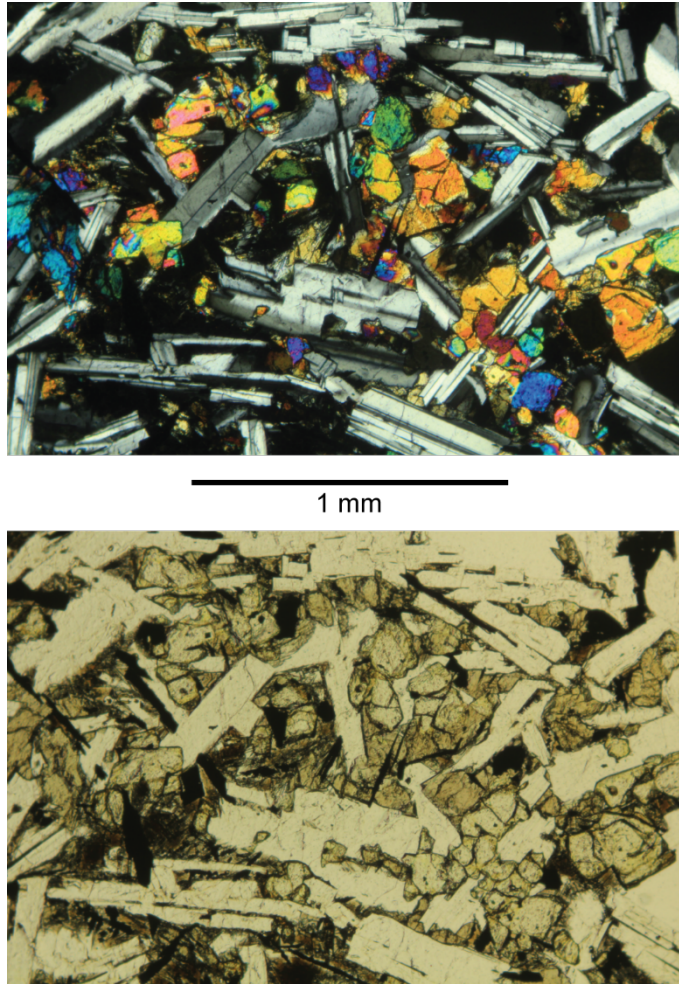


Figure 2. Basalt sample from the Eastern Snake River Plain in cross- and plane-polarized light. Sample is fully crystalline (i.e., there is no evidence of glass).

A 0.92 mol NaCl/kg solution with dissolved CO₂ (1 molal NaCl) was prepared as the experimental brine using laboratory-grade NaCl, deionized (DI) water, and industrial-grade CO₂. The flow system was purged of oxygen before experimental fluid was added. Nitrogen flowed through the flow system, and residual oxygen was also removed from the upstream separator by going through cycles of exposing it to ~60 bar of CO₂ pressure and then releasing the CO₂ and ultimately pulling a vacuum. After this, nitrogen was bubbled through experimental fluid for at least 3 h before it was pumped to the upstream separator using a HPLC pump. A syringe pump was then used to pressurize the brine solution. After CO₂ was transferred from a cylinder to

another syringe pump, a known volume of liquid CO₂ was added to the brine to achieve a CO₂ concentration of 0.6 mol/kg solution (0.65 molal CO₂), which is ~83% of the saturation concentration at experimental temperature and pressure conditions (Duan et al., 2006; Duan and Sun, 2003).

Four experiments were conducted that lasted from 0.51-32.81 days to assess feedbacks between chemical reactions and flow fields during basalt alteration in a CO₂-rich setting. Two experiments used a flow rate of 0.1 ml/min, and two used a flow rate of 0.01 ml/min. In reality, flow rates were 0.104 and 0.0104 ml/min in the heated pressure vessel (experimental solution had a density 0.966 g/ml, calculated using Duan et al. (2008)), but we refer to flow rates from the room temperature pumps of 0.1 and 0.01 ml/min for simplicity. The reaction cell was heated to 150°C for all experiments, using outlet pore-fluid and confinement pressures of 150 and 200 bar, respectively. Just before these experiments commenced, DI water was pumped through each core for several hours to develop steady-state fluid pressure gradients. At the end of each experiment, DI water flow displaced experimental brine from all cores. A series of flow rates was used during DI water flow pre- and post-experiment to provide more precise initial and final permeabilities. An attempt was also made to remove oxygen from DI water that flowed through the cores by bubbling nitrogen through the water for at least 3 h before it was added to the system.

Fluid samples were periodically collected as experiments proceeded. Samples were filtered with a 0.2 µm filter, acidified with trace metal grade HCl, and further diluted before they were analyzed for major cations and trace elements with an ICP-OES and ICP-MS, respectively. CO₂ concentration was determined using a manometric technique (Luhmann et al., 2013, 2014; Luquot et al., 2012). The first fluid sample collected during each experiment was corrected for

dilution from mixing of DI water and experimental solution using Na^+ analyses, which is justifiable since the Na^+ concentration of the experimental solution (0.92 mol/kg) is much larger than any change in Na^+ concentration that would result from interaction with the cores.

Saturation indices were calculated and reaction modeling was conducted using Geochemist's Workbench (GWB, version 10.0.3; Bethke and Yeakel, 2015), employing a database that is largely consistent with SUPCRT92 (Johnson et al., 1992). Modifications and additions to the database included revised thermodynamic data for Al-bearing minerals and aqueous species (Tagirov and Schott, 2001), quartz, and $\text{H}_4\text{SiO}_4(\text{aq})$ (Stefansson, 2001), as discussed in Tutolo et al. (2014), and metal complex equilibria (Sverjensky et al., 1997) and solubility constants for plagioclase (Arnórsson and Stefansson, 1999), dawsonite (Ferrante et al., 1976), and analcime (Johnson et al., 1982; Robie and Hemingway, 1995). Furthermore, equilibrium constants for carbonic acid ionization and sodium bicarbonate and carbonate complexes from Stefansson et al. (2013) and magnesium bicarbonate and carbonate complexes from Stefansson et al. (2014) were incorporated. Finally, the database was modified to experimental temperature and pressure conditions using the DBCreate program (Kong et al., 2013).

Mass balance (m_b) calculations enable comparison between actual mass changes and mass changes calculated using outlet major element fluid chemistry:

$$m_b = -\sum_i^j M_i Q_m \int_{t'=0}^{t'=t} \Delta C_i(t') dt' \left(1 + \frac{N_O M_O}{N_i M_i}\right), \quad (2)$$

where M_i is the atomic mass of element i , Q_m is the mass fluid flow rate, ΔC_i is the outlet concentration of element i , t is time, N_O is the number of oxygen atoms in the oxide that corresponds to element i , M_O is the atomic mass of oxygen (15.9994 g/mol), and N_i is the number of atoms of element i in the oxide that corresponds to element i . We employ the oxide formula

for each of the elements as is provided in Table 1, and all elements in Table 4 (i.e., major chemistry, not trace elements) were used in the mass balance calculations except for Na because of the larger uncertainty in Na concentrations that arise with the 1 molal NaCl solution.

Pristine and post-experimental basalt were imaged using a JEOL JSM-6500F scanning electron microscope (SEM), with an accelerating voltage of 15 kV and a probe current of 5 nA. The SEM imaged sections of the very upstream and downstream ends of the post-experimental cores from Experiments 2 and 4 (i.e., the longest experiment for each of the two different flow rates) to ensure that pictures portrayed reacted surfaces rather than artifacts that arise from cutting or breaking of post-experimental samples. While SEM observations necessarily focus on specific sections of the experimental samples, the companion paper portrays dissolution and precipitation throughout all four cores from XRCT datasets (Luhmann et al., in review). A JEOL JXA-8900 electron microprobe was used to analyze secondary mineral grains.

A pristine basalt sample and portions of the upstream and downstream ends of all four experimental cores were powdered for low- and high-temperature magnetic analyses to assess change from experimental alteration. Room temperature hysteresis loops were obtained in a vibrating sample magnetometer (Princeton Measurements Corporation 3900) using an electromagnet to produce fields up to 1 T. Low-temperature (20—300 K) remanent magnetization curves were obtained with a SQUID magnetometer (Quantum Design MPMS-XL). Remanent magnetization was acquired in a 2.5 T field. High-temperature susceptibility measurements were made using a variable temperature low-field AC Susceptometer (AGICO KLY2). Susceptibility was measured during heating-cooling cycles at 10 °/min up to 620-650°C in flowing argon to reduce the effects of oxidation.

3. Results

Core permeability increased for both experiments at the higher flow rate (1 and 2) and decreased for the experiments at the lower flow rate (3 and 4) (Figure 3 and Table 3). Core permeability changes were generally reproducible during Experiments 3 and 4, but there was a significant difference between the permeability increases during Experiments 1 and 2. Over the 2.7 day-long experiment, the permeability in Experiment 2 increased by a factor of less than two. In contrast, the permeability in Experiment 1 increased by more than an order of magnitude, even though the experiment lasted only a half day. While the final permeabilities of the cores from Experiments 3 and 4 were slightly lower than the initial permeabilities, permeability of both cores increased at the end of the experiments after initial reductions. In an ancillary, 9.5-day experiment run with DI water at 21°C and 150°C (sequentially for 2.6 and 6.9 days, respectively), permeability decreased through time ($5.6 \times 10^{-16} \text{ m}^2$ to $1.0 \times 10^{-17} \text{ m}^2$), with the rate of permeability decrease increasing at the higher temperature. This Arrhenius-style behavior in the permeability measurements is consistent with the chemical reactions being the primary cause of permeability changes during our presented experiments.

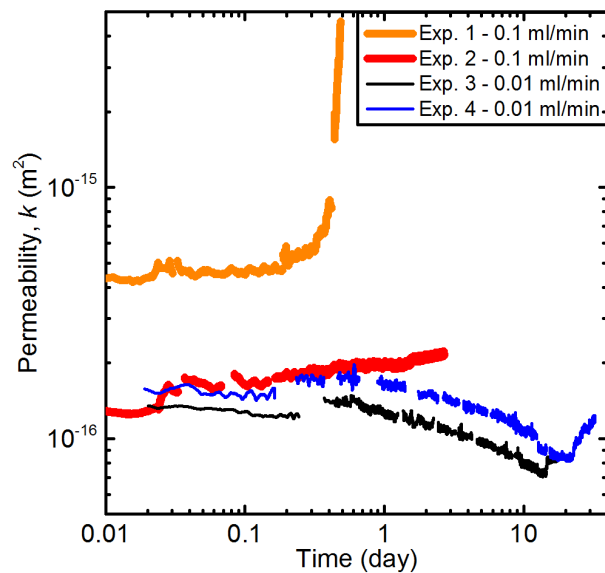


Figure 3. Permeability decreased for both experiments at the lower flow rate (Experiments 3 and 4), but permeability increased at the later stages of the experiments following initial decreases. Permeability increased for both experiments at the higher flow rate (Experiments 1 and 2), but the permeability increase during Experiment 1 was much greater than the permeability increase in Experiment 2.

Table 3
Experiment details and dimensions and mass and permeability changes of experimental cores.

Experiment	Flow rate (ml/min)	Duration (day)	Core diameter (cm)	Core length (cm)	Pre-experiment mass (g)	Core mass change (g)	Mass balance (no Na) change (g)	Initial permeability (m ²)	Final permeability (m ²)
1	0.1	0.51	1.28	2.59	8.464	-0.032	-0.03	4.4×10^{-16}	9.8×10^{-1}
2	0.1	2.74	1.28	2.53	8.740	-0.150	-0.14	1.27×10^{-16}	2.18×10
3	0.01	19.62	1.28	2.59	8.935	-0.146	-0.18	1.49×10^{-16}	9.3×10^{-1}
4	0.01	32.81	1.28	2.61	8.997	-0.223	-0.34	1.48×10^{-16}	1.19×10

Flow rate caused a first order difference for the major components in the outlet fluid chemistry (Figure 4, Tables 4 and 5). At the lower flow rate, Fe concentration initially increased up to a maximum of 2.5 mmol/kg and then decreased with reaction progress. Mg generally increased with time during the lower flow rate experiments, yielding concentrations up to ~6 mmol/kg. Following a brief initial decrease in concentration, Si increased up to ~7 mmol/kg as these experiments proceeded. In contrast, Fe, Mg, and Si were relatively stable at the higher flow rate. After an initial relatively high concentration, many elements decreased dramatically for both flow rates (Ba, Ca, Cu, K, Mn, and Sr). Fluid-rock reaction consumed dissolved CO₂ to produce an increase in pH. The initial, in-situ calculated pH of the experimental solution was 3.3, and in-situ pH ranged from 4.2 to 5.2 downstream of the basalt cores. In-situ pH was calculated by imposing charge balance and distribution of aqueous species constraints using Geochemist's Workbench (GWB; Bethke and Yeakel, 2015). In general, the fluid chemistry from each set of experiments conducted at the same flow rate yielded reproducible results.

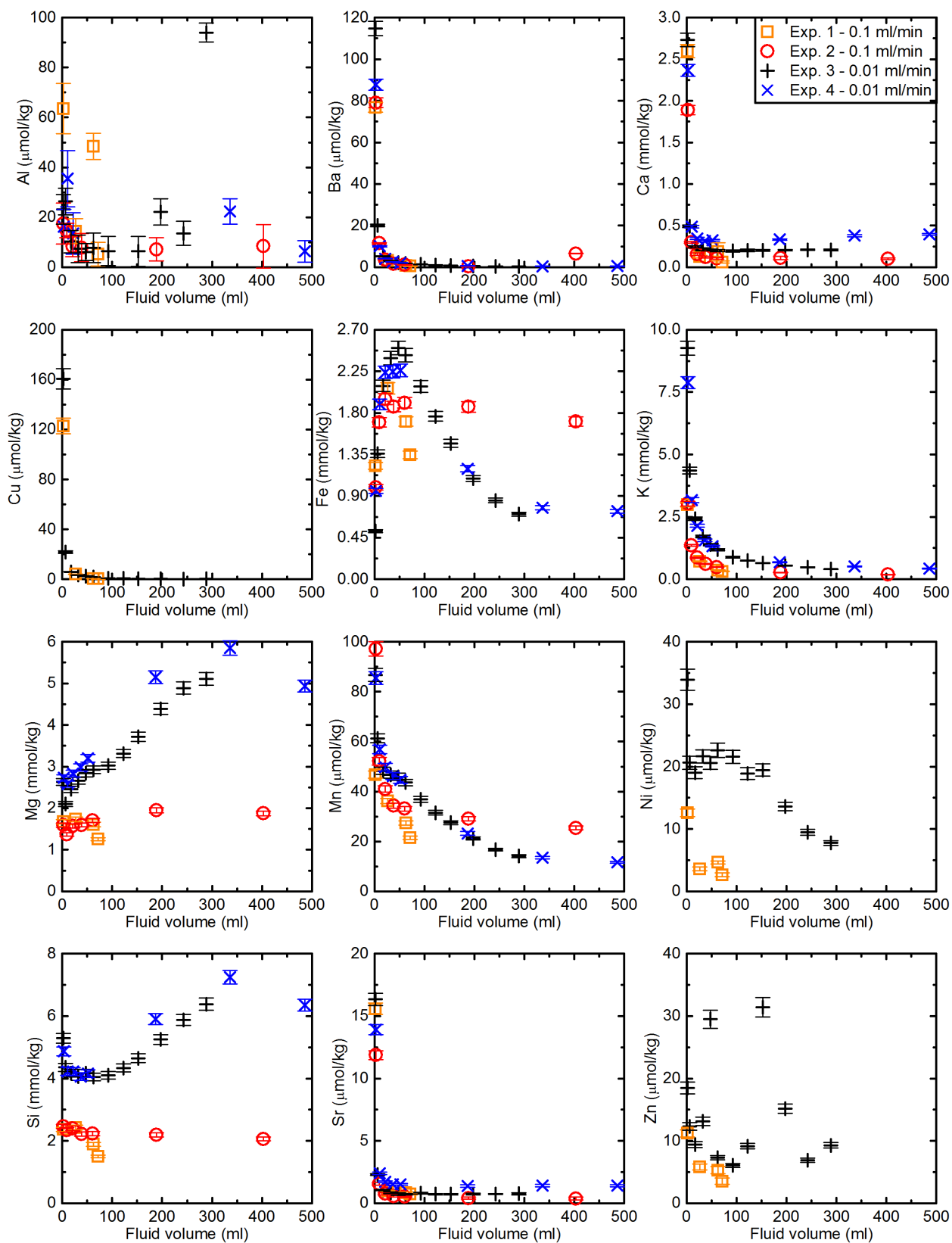


Figure 4. Experiments at each flow rate produced unique trends in Fe, Mg, and Si, and these trends were generally reproducible among experiments at the same flow rate. At the lower flow rate (0.01 ml/min), Fe briefly increased and then decreased with further reaction progress. Si underwent opposite trends of Fe concentrations, and Mg generally increased continuously at this lower flow rate. Other elements decreased dramatically with reaction progress at both flow rates (Ba, Ca, Cu, K, Mn, and Sr). Error bars indicate 2 σ error.

Table 4. Outlet major element chemistry.

Time (min)	pH ^a	CO ₂ (mol /kg) ^b	Al ³⁺ (μ mol /kg)	Ba ²⁺ (μ mo l/kg)	Ca ²⁺ (mmol/ kg)	Fe ²⁺ (mmo l/kg)	K ⁺ (mmol /kg)	Mg ²⁺ (mmol /kg)	Mn ²⁺ (μ mol/ kg)	Na ⁺ (mmo l/kg)	Si (mmo l/kg)	Sr ²⁺ (μ mol /kg)
<i>Experiment 1: 0.1 ml/min</i>												
pre ^c	4.91	-	111	<DL	0.024	<DL	0.099	0.042	<DL	0.55	1.23	0.11
19-dil		0.42	54	65	2.21	1.04	2.54	1.42	40	760	2.02	13.2
19-corr	4.74	0.50	64	77	2.60	1.23	2.98	1.67	47	890	2.37	15.6
255	4.47	0.55	14 ^e	3.2	0.13	2.07	0.72	1.73	36	900	2.43	0.98
604	4.38	0.60	48	0.86	0.2 ^d	1.71	0.37	1.61	27.3	880	1.89	0.83
687	4.24	0.63	5 ^d	0.53	0.06	1.35	0.315	1.25	21.4	890	1.50	0.72
<i>Experiment 2: 0.1 ml/min</i>												
23-dil		0.41	16 ^d	71	1.70	0.89	2.72	1.43	87	820	2.21	10.7
23-corr	4.72	0.45	17 ^d	79	1.89	0.99	3.03	1.59	97	910	2.46	11.9
89	4.50	0.49	15	11.5	0.297	1.70	1.36	1.37	52	920	2.35	1.6
203	4.49	0.50	8 ^e	3.5	0.15	1.95	0.87	1.57	41	910	2.40	0.76
370	4.46	0.52	8 ^d	1.68	0.12	1.87	0.61	1.60	34	900	2.22	0.57
583	4.47	0.51	<DL	1.1	0.11	1.91	0.48	1.71	33	910	2.23	0.52
1814	4.45	0.54	7 ^d	0.4 ^e	0.11	1.86	0.269	1.95	29.1	910	2.20	0.41
3874	4.45	0.51	8 ^d	0.2 ^d	0.10	1.71	0.185	1.88	25.4	920	2.06	0.4
<i>Experiment 3: 0.01 ml/min</i>												
199-dil		0.24	20	97	2.32	0.44	7.9	2.23	74	760	4.5	13.9
199-corr	5.15	0.29	23	115	2.73	0.52	9.3	2.63	87	890	5.3	16.3
594	4.85	0.33	26	20.1	0.49	1.36	4.4	2.10	61	890	4.4	2.30
1659	4.79	0.37	10 ^e	5.3	0.24	2.09	2.42	2.45	48	920	4.2	1.06
3109	4.78	0.39	7 ^d	3.1	0.22	2.39	1.71	2.66	47	910	4.1	0.84
4557	4.79	0.39	6 ^d	2.3	0.21	2.50	1.39	2.84	46	910	4.2	0.75
5990	4.75	0.41	8 ^d	1.80	0.20	2.43	1.18	2.92	44	890	4.1	0.71
8893	4.71	0.43	6 ^d	1.3	0.20	2.09	0.89	3.02	37	880	4.1	0.79
11767	4.69	0.44	<DL	1.02	0.20	1.76	0.75	3.3	31.5	880	4.3	0.73
14650	4.67	0.46	6 ^d	0.79	0.20	1.47	0.65	3.7	27.5	880	4.6	0.72
18960	4.68	0.47	22	0.56	0.203	1.09	0.55	4.4	21.2	880	5.3	0.73
23322	4.68	0.49	14	0.43	0.209	0.85	0.48	4.9	16.8	880	5.9	0.74
27774	4.66	0.50	94	0.3	0.21	0.70	0.40	5.1	14.1	900	6.4	0.76
<i>Experiment 4: 0.01 ml/min</i>												

<i>276-dil</i>		<i>0.35</i>	<i>13^d</i>	<i>73</i>	<i>1.97</i>	<i>0.80</i>	<i>6.6</i>	<i>2.27</i>	<i>71</i>	<i>750</i>	<i>4.1</i>	<i>11.6</i>
276-corr	4.96	0.42	16 ^d	88	2.36	0.96	7.9	2.73	86	900	4.9	13.9
1014	4.71	0.48	40	10.0	0.49	1.89	3.2	2.58	57	910	4.2	2.4
2094	4.70	0.50	14 ^d	4.1	0.35	2.24	2.14	2.84	50	910	4.2	1.72
3536	4.68	0.51	<DL	2.5	0.31	2.25	1.56	2.98	46	890	4.1	1.52
4973	4.68	0.52	<DL	2.0	0.32	2.26	1.32	3.20	45	890	4.2	1.51
17943	4.69	0.54	<DL	0.60	0.332	1.20	0.68	5.2	23.2	900	5.9	1.4
32331	4.72	0.51	22	0.39	0.38	0.77	0.51	5.9	13.5	910	7.2	1.42
46737	4.66	0.51	6 ^d	0.5	0.40	0.74	0.43	4.9	11.6	920	6.3	1.40

Rows with italicized values were corrected for dilution (using Na⁺ analyses) that occurred at the beginning of all 4 experiments. DL = detection limit, *dil* = diluted by DI water at beginning of experiment, corr = corrected for dilution.

^aDetermined from speciation calculations.

^bMeasured using manometric technique.

^cSample was collected during DI water flow at 150°C before the experiment began (pre = pre-experiment sample).

^dAnalyzed value is not larger than 2× the 2σ error.

^eAnalyzed value is not larger than 3× the 2σ error.

328

329 **Table 5. Outlet trace element chemistry.**

Time (min)	Li	V	Cr	Ni	Cu	Zn	As	Rb	Mo	Cd	Sn	Sb	Cs	Pb	U
	(μm ol/kg g)	(nmo l/kg)	(μm ol/kg)	(μm ol/kg)	(μmo l/kg)	(μm ol/kg g)	(nmo l/kg)	(nmol /kg)	(nm ol/kg)	(nm ol/kg)	(nmo l/kg)	(nm ol/kg)	(nm ol/kg)	(nm ol/kg)	(nm ol/kg)
<i>Experiment 1: 0.1 ml/min</i>															
pre ^a	0.4 ^b	270	<DL	0.23 ^c	<DL	0.4	<DL	150	310	<DL	40 ^c	40 ^c	25	<DL	<DL
19-dil	10.3	140	0.7	10.7	104	9.5	<DL	2200	780	60 ^c	40 ^c	120	760	320	<DL
19-corr	12.1	170	0.9	12.6	123	11.2	<DL	2600	920	70 ^c	50 ^c	140	890	370	<DL
255	3.1	100	1.0	3.6	4.1	5.8	<DL	200 ^b	1090	4 ^b	30 ^c	120	21 ^c	270	0.8
604	2.4	70 ^b	1.0	4.6	0.50	5.3	<DL	110 ^c	860	<DL	20 ^b	60 ^b	4 ^b	200	0.2 ^b
687	2.1	180	1.1	2.6	0.29	3.5	<DL	80 ^b	670	<DL	17 ^b	90 ^c	<DL	99	<DL
<i>Experiment 3: 0.01 ml/min</i>															
199-dil	29	800	1.10	29	136	15.7	50 ^b	3400	160	130		<DL	1050	132	0.8 ^b
199-corr	34	1000	1.30	34	161	18.5	60 ^b	4000	190	160		<DL	1230	156	0.9 ^b
594	15	900	1.5	21	22	12.3	90 ^c	1100	230	33		<DL	130	210	0.6 ^b
1659	8.8	90	0.78	19	6.0	9.4	300 ^c	2300	360	12 ^c	12 ^c	14 ^b	580	183	1.8
3109	7.0	80	0.69	21.6	3.3	13.1	240	1500	490	9 ^c	<DL	22	310	141	1.2 ^c
4557	5.4	49	0.90	21	2.5	29	190 ^c	1200 ^c	550	7 ^c	<DL	<DL	110	180	<DL
5990	5.0	65	0.81	23	1.74	7.3	30 ^b	240	650	9 ^b	16	29	4	140	0.9
8893	3.2	80	0.74	22	0.80	6.1	20 ^b	170 ^b	820	8 ^c	21	70	3.2	180	0.7 ^c
11767	3.2	62	0.73	18.9	0.81	9.1	20 ^b	140 ^b	810	8 ^c	<DL	21 ^c	2.6	150	0.5 ^c
14650	3.7	40 ^c	1.24	19	0.52	31	<DL	100 ^b	810	4 ^b	12	32	<DL	93	<DL
18960	4.4	60 ^c	0.54	13.6	0.54	15.1	10 ^b	<DL	720	8 ^c	<DL	50	<DL	66	<DL
23322	2.2	61	0.59	9.4	0.09	6.9	10 ^b	<DL	650	11	13	68	1.2 ^b	47	0.17
27774	6.4	60	0.65	7.8	0.26	9.3	<DL	<DL	530	6 ^b	<DL	70	<DL	52	<DL

330 Rows with italicized values were corrected for dilution (using Na⁺ analyses) that occurred at the beginning of all 4
331 experiments. pre = pre-experiment, DL = detection limit, *dil* = diluted by DI water at beginning of experiment, corr
332 = corrected for dilution.

333 ^aSample was collected during DI water flow at 150°C before the experiment began (pre = pre-experiment sample).

334 ^bAnalyzed value is not larger than 2× the 2σ error.

335 ^cAnalyzed value is not larger than 3× the 2σ error.

Outlet fluids were generally supersaturated with Al-rich phases that include kaolinite, analcime, diaspore, K-feldspar, and gibbsite (Figure 5). The saturation index, Ω , is given by the following equation

$$\Omega = \frac{Q}{K}, \quad (3)$$

where Q is the ion activity product and K is the equilibrium constant. All samples were near saturation with respect to quartz and amorphous SiO_2 , with saturation indices slightly lower for the samples from Experiments 1 and 2 at a flow rate of 0.1 ml/min than they were for the samples from Experiments 3 and 4 at a flow rate of 0.01 ml/min. Finally, samples collected during all four experiments were saturated or supersaturated with respect to siderite and near saturation with respect to dawsonite. However, all other carbonates were generally undersaturated, with saturation indices decreasing from magnesite to dolomite to calcite. For dolomite and calcite, the $\log \Omega$ was less than -3 for most samples from the experiments with the higher flow rate (1 and 2).

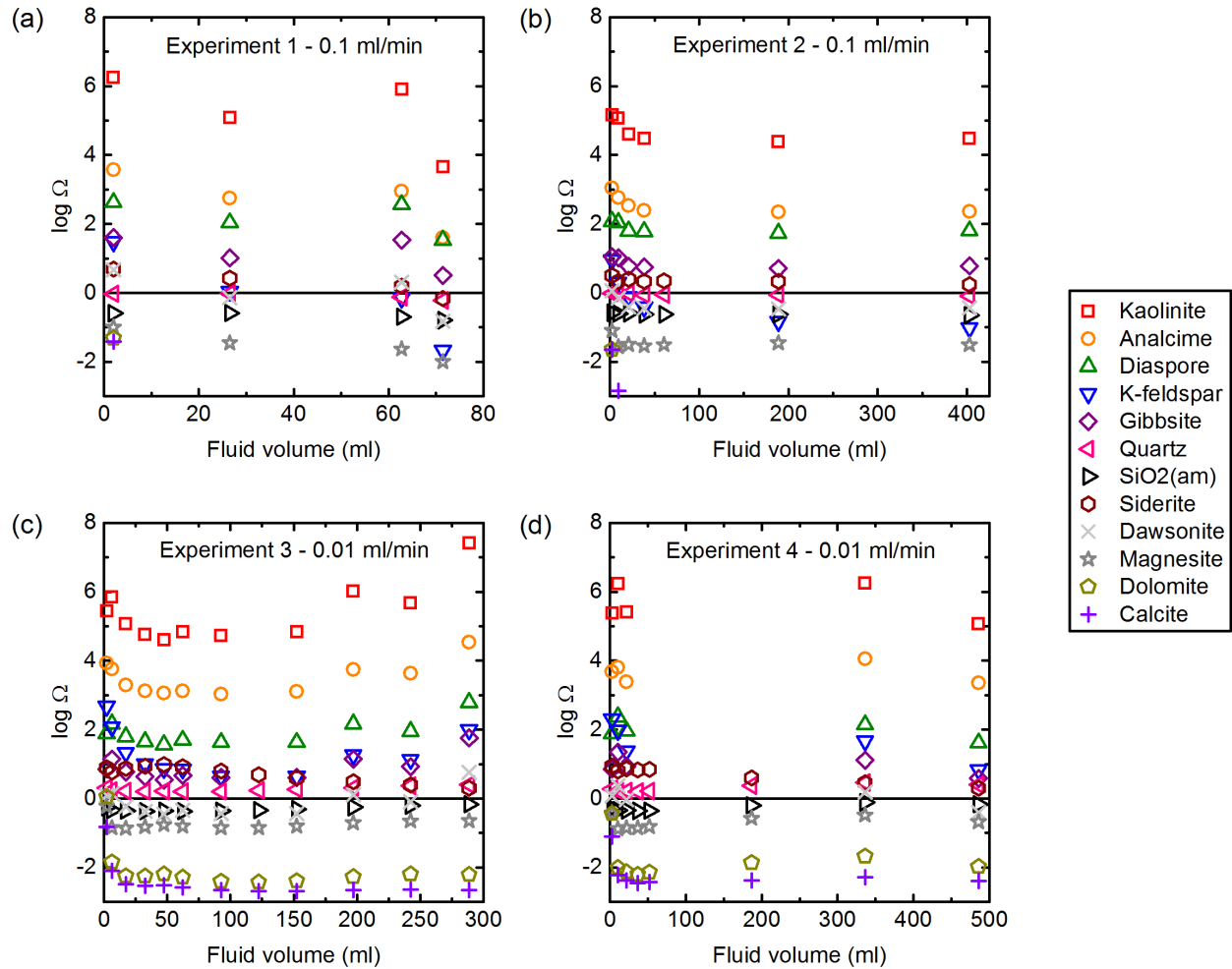


Figure 5. Saturation index, Ω , as a function of fluid volume for Experiments (a) 1, (b) 2, (c) 3, and (d) 4. Many Al-rich secondary phases were supersaturated, but the only carbonate that was supersaturated was siderite.

Mass balance calculations incorporating oxides of all elements except Na in Table 4 specify core mass reductions of 0.4% to 3.7%, while core mass decreases were actually 0.4% to 2.5% (Table 3). There is good agreement between core mass changes and mass balance calculations for the higher flow rate experiments (0.4% and 0.4% for Experiment 1 and 1.6% and 1.7% for Experiment 2, respectively). In contrast, core mass reductions were less than mass balance reductions for the lower flow rate experiments (1.6% and 2.0% for Experiment 3 and 2.5% and 3.7% for Experiment 4, respectively), with a larger difference in the core from

Experiment 4 (which lasted 13.19 days longer than Experiment 3). This potentially suggests a net uptake of Na into secondary phases within these two experimental cores, which increases with reaction time.

SEM images portrayed effects of both dissolution and precipitation on post-experimental cores when compared to the pristine sample (Figure 6). Pristine basalt was generally characterized by relatively clean grain surfaces (Figure 6a). Evidence for dissolution included etched mineral grains, such as the plagioclase crystal shown in Figure 6c. EDS analyses indicated that the etched outer portion of the plagioclase crystal contained Na and K, whereas the inner portion of crystal appeared unreacted and contained more Ca than the outer portion of the crystal. In contrast, the upstream portion of the cores from Experiments 3 and 4 portrayed secondary mineralization. A secondary phase observed on the reacted core from Experiment 3 was enriched in Al and Si (and some Na and Ca) (Figure 6b), while another secondary phase identified on the reacted core from Experiment 4 portrayed a needle-like morphology and contained more Al than Si (Figure 6d).

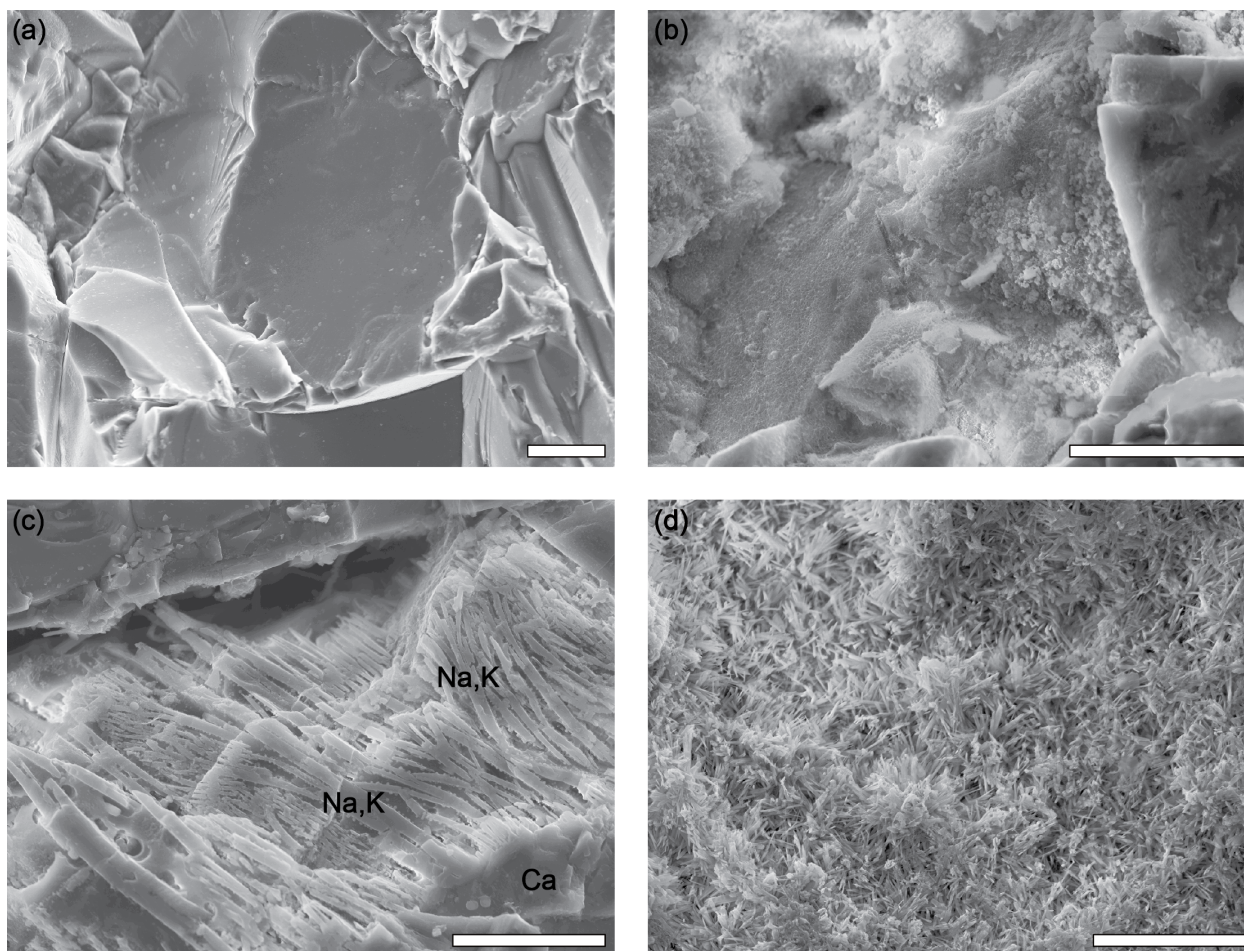


Figure 6. SEM pictures of (a) pristine and (b-d) post-experimental basalt. (a) Pristine grains in basalt core are relatively clean, as illustrated with this grain of olivine. (b) An Al and Si-rich secondary phase (with some Na and Ca) was observed on the upstream end of the post-Experiment 3 core. (c) The plagioclase crystal portrayed evidence of dissolution on the upstream end of the post-Experiment 4 core, with dissolution primarily focused on the outer portion of the mineral grain that was relatively rich in Na and K. (The letters Na and K and Ca indicate relative enrichment of these elements from EDS spot analyses). (d) An Al-rich phase with a needle-like morphology was identified on the upstream end of the post-Experiment 4 core. The scale bar in each image is 10 μm .

In addition to the secondary mineralization that occurred throughout the cores, secondary mineralization was identified on the PEEK retainer ring immediately downstream of the cores from Experiments 3 and 4 (see 3D segmentations of XRCT data illustrating precipitation in Figure 2c-d in Luhmann et al. (in review)). Figure 7a illustrates the morphology of the secondary phase that covered a portion of the outlet PEEK retainer ring from Experiment 4. Two grains from this ring were analyzed with an electron microprobe (Figure 7b) and indicated a composition primarily of Fe and O (Table 6). The Grain 1 analysis suggests an Fe_2O_3 -rich composition, yielding a total wt% of nearly 100% (Table 6). While the grains looked similar (Figure 7a), there was possibly some $\text{FeO}(\text{OH})$ on the surface of the Fe_2O_3 -dominated particle of the Grain 2 analysis, producing a total wt% less than 100% for the analysis, since H cannot be analyzed by the microprobe (Table 6). XRCT indicated that the Fe_2O_3 -rich phase was confined to the downstream face of the cores and the downstream PEEK retainer rings (Luhmann et al., in review).

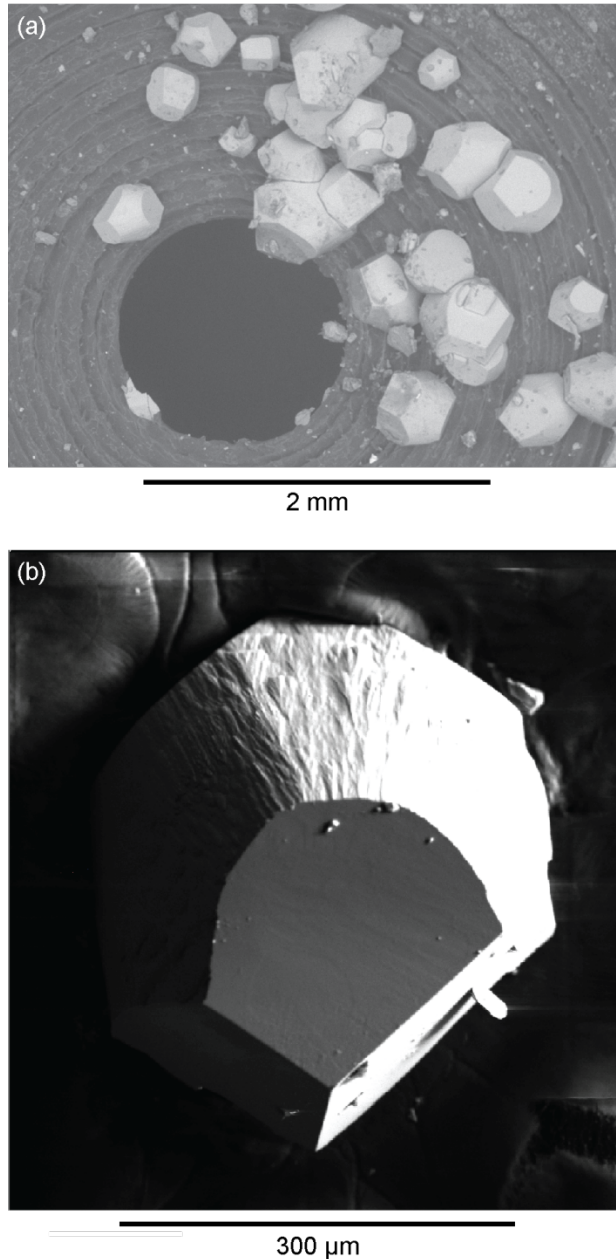


Figure 7. (a) SEM image of secondary mineralization on the outlet PEEK retainer ring from Experiment 4. The entire ring was 1.3 cm in diameter, and secondary mineralization occurred on the cone surface of the ring. The picture shows the hole drilled through the ring which allows fluid to pass through. (b) Electron microprobe analyses of two grains from the PEEK retainer ring indicated an Fe_2O_3 -rich composition. The Grain 1 analysis in

Table 6 was conducted on the relatively flat, horizontal surface of the grain portrayed in (b).

Table 6
Major oxide composition of secondary precipitation.

Oxide	Grain 1	Grain 2
	wt%	wt%
Al ₂ O ₃	0.18	-
CaO	0.27	0.22
Fe ₂ O ₃	93.64	88.56
MgO	2.59	2.53
MnO	0.90	1.05
P ₂ O ₅	0.21	0.29
SiO ₂	1.77	1.03
Total	99.56	93.68

Magnetization measurements indicated a decrease in the saturation magnetization, M_s , of all post-experimental samples (Table 7), likely due to dissolution of titanomagnetite in the cores. The decrease ranged from 7.4% to 24.2% when comparing upstream and downstream sections from all four post-experimental cores to the pristine sample, with the most significant decrease for the upstream end of the longest experiment at the lower flow rate (Exp. 4). The decrease was larger at the downstream end of the experiments at the higher flow rate (1 and 2) and larger at the upstream end of the experiments at the lower flow rate (3 and 4). In addition, there was no direct evidence for siderite based on low-temperature magnetic measurements (e.g., Frederichs et al., 2003), although the strongly magnetic titanomagnetite would likely dwarf any potential siderite signal.

Table 7
Changes in saturation magnetization, M_s , from hysteresis measurements and susceptibility, χ , after heating to 620-650°C.

Experiment	Change in M_s (%)	Change in χ (%)
1	-12.4 (upstream)	5.96 (upstream)
	-22.4 (downstream)	7.69 (downstream)
2	-8.0 (upstream)	15.2 (upstream)
	-11.8 (downstream)	0.00 (downstream)
3	-17.1 (upstream)	83.0 (upstream)
	-7.4 (downstream)	18.0 (downstream)

4	-24.2 (upstream)	249 (upstream)
	-23.6 (downstream)	138 (downstream)

421

422 During heating to 620-650°C and cooling to room temperature, upstream and

423 downstream samples from Experiments 3 and 4 showed irreversible χ behavior (Figure 8). Upon

424 cooling of the post-experimental powders from Experiments 3 and 4, χ increased, with upstream

425 samples showing much larger χ increases than downstream samples (Figure 8, Table 7). After

426 heating the saturation magnetization increased by a factor of 5 for experiment 4, indicating a

427 strongly magnetic phase was produced during heating. The irreversibility likely arose from the

428 production of impure magnetite during the high-temperature susceptibility measurements, where

429 magnetite was converted from either an Fe-bearing paramagnetic secondary phase (possibly

430 clay) or perhaps primary olivine and/or pyroxene crystals damaged from experimental alteration

431 during the lower flow rate experiments. In contrast, upstream and downstream samples from

432 Experiment 1 and 2 showed nearly reproducible χ behavior upon heating and cooling, which is

433 practically indistinguishable from the pristine sample response (Figure 8). Thus, experimental

434 flow rate caused a fundamental difference in the susceptibility response of the post-experimental

435 magnetic analysis. Whereas χ increased up to 249% after heating to 620-650°C for the faster

436 flow rate experiments (3 and 4), the lower flow rate experiments (1 and 2) produced no change to

437 15.2% change in χ (Table 7). The sample from the longer-lasting Experiment 4 underwent a

438 larger change than the sample from the shorter Experiment 3.

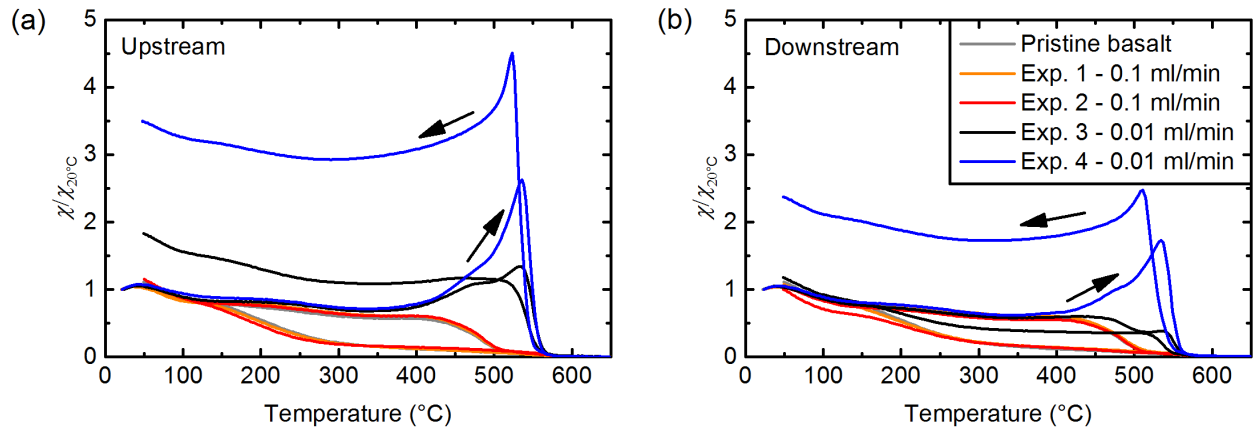


Figure 8. Normalized susceptibility ($\chi/\chi_{20^{\circ}\text{C}}$, where $\chi_{20^{\circ}\text{C}}$ is χ measured at 20°C) for pristine basalt and basalt from the (a) upstream and (b) downstream sections of all post-experimental cores. The susceptibility of the samples from the lower flow rate experiments (1 and 2) increased significantly upon heating, likely caused by the conversion of either an Fe-bearing secondary phase or a damaged Fe-rich primary phase to a magnetic phase. The magnetic phase associated with the increase of susceptibility has a Curie temperature ($T_c \sim 545^{\circ}\text{C}$) slightly less than for pure magnetite ($T_c = 575^{\circ}\text{C}$) suggesting the magnetite contains minor amounts of impurity cations. Arrows are shown on the Experiment 4 sample curves to indicate direction during heating-cooling cycles.

4. Discussion

4.1. Chemical evolution

Each set of experiments at the two different flow rates generally yielded reproducible results for outlet fluid chemistry (Figure 4, Table 4), and dissolution profiles suggest that most of the dissolution occurred at the upstream ends of the cores (Luhmann et al., in review). Except for Fe, fluid concentrations of the major elements (Ca, K, Mg, and Si) were higher during Experiments 3 and 4, indicating an increase in fluid concentration with residence time for these

components. The decrease in dissolved Fe during Experiments 3 and 4 likely resulted from the precipitation of the Fe₂O₃-rich phase at the downstream end of the cores, which presumably formed upon exiting the cores because of the additional residence time for that portion that allowed enhanced mineralization. Since the Fe₂O₃-rich secondary phase was focused on the downstream face and the downstream PEEK retainer ring, the precipitation of Al-rich phases (Figure 6b and d) was likely responsible for the measured permeability reduction during Experiments 3 and 4, where secondary mineralization made pore throats smaller even in the midst of significant dissolution. Furthermore, SEM images suggest Na mobility with the plagioclase dissolution (Figure 6c) and slight Na incorporation into secondary Al- and Si-rich phases (Figure 6b), and mass balance constraints suggest a net Na incorporation into the experimental cores from the lower flow rate experiments (Table 3). The gradual permeability decrease during the DI water run suggests that permeability changes were caused by chemical reactions, especially with the faster rate of permeability decrease at the higher temperature. If fine particle migration were responsible for permeability changes, we would have expected much of the permeability reduction to occur at the beginning of the DI water run. Fe, Mg, and Si outlet concentrations for Experiments 1 and 2 were generally more stable than the concentrations during Experiments 3 and 4, where fluid concentrations increased or decreased as a function of time or fluid volume that passed through the core. However, it is also important to note the decrease in dissolved Ca, Fe, Mg, Mn, and Si during the end of Experiment 1. These decreases occurred during the significant rise in permeability at the end of the experiment, and the fluid chemistry and permeability data together indicate the opening of flow paths from dissolution that produced this increase in permeability that subsequently limited fluid-rock reaction. See Luhmann et al. (in review) for a detailed discussion of permeability changes.

Given that dissolution rates for olivine (e.g., Chen and Brantley, 2000; Hänchen et al., 2006; Pokrovsky and Schott, 2000; Rosso and Rimstidt, 2000; Wogelius and Walther, 1991) are higher than they are for either pyroxene (Chen and Brantley, 1998; Knauss et al., 1993; Oelkers and Schott, 2001) or plagioclase (Chou and Wollast, 1985; Gudbrandsson et al., 2014; Knauss and Wolery, 1986) in the pH range of 3-5 (see Figure 1 in Gudbrandsson et al., 2011), one source of the relatively high Fe, Mg, and Si concentrations result from olivine dissolution. Other mineral phases also likely contribute to the dissolved flux of Fe, Mg, and Si. For example, the reduction in M_s provided by the magnetization analyses indicates some dissolution of titanomagnetite, and pyroxene dissolution may have contributed to the dissolved load. In an analysis of natural waters in Iceland with a pH range of ~6-10, Gíslason and Arnórsson (1993) demonstrated the greater thermodynamic drive for basalt dissolution at lower pH, although they noted that decreasing pH has the greatest effect on olivine dissolution in particular. The elevated Fe, Mg, and Si concentrations resulted from the experimental fluid having very little residence time in the cores. With the post-experimental porosities provided in Table 3, residence time at the end of Experiments 1 and 3 was ~5 and ~39 minutes, respectively. Even with our cone-shaped retainer ring at both ends of the core (that allows additional fluid-rock reaction), an additional 2 or 20 minutes of reaction at most would occur for experiments using flow rates of 0.1 or 0.01 ml/min, respectively, since each cone can accommodate ~0.1 ml of fluid. Thus, reaction between CO₂-charged brine and crystalline basalt was able to produce Fe and Mg concentrations up to ~2 mmol/kg in seven minutes for the experiments at the faster flow rate (1 and 2). Furthermore, it is noteworthy that the magnitude of Fe and Mg outlet concentrations were comparable, to the extent that Fe concentrations from several samples from the faster flow rate experiments (1 and 2) were higher than the Mg concentrations. In addition to olivine

dissolution, the dissolution of titanomagnetite (and perhaps Fe-rich pyroxene) would provide an additional Fe source and account for the elevated dissolved Fe concentrations. It is also possible that Fe was more mobile than Mg during the dissolution of olivine. Previous research has noted faster dissolution kinetics for fayalite than forsterite (Wogelius and Walther, 1992; Daval et al., 2010), so the fayalite component of the olivine may have overexpressed itself beyond what would be expected based on dissolution of an ideal solid solution. Alternatively, we cannot rule out that compositional constraints of the olivine were responsible for the Fe and Mg aqueous concentrations. Elevated Fe has been noted following CO₂ injection into a sandstone of the Frio Formation; reaction caused an increase in dissolved Fe (up to 20 mmol/kg), Mn, Zn, Pb, and Mo, likely resulting from dissolution of iron oxyhydroxides and/or corrosion of the pipe and well casing (Kharaka et al., 2009). Our elevated Fe concentrations arise from dissolution of the basalt rather than the experimental flow system, as our reaction cell incorporates corrosion-resistant titanium flow pieces and previous experiments using the same reaction cell, temperature, flow rate, and fluid composition produced Fe concentrations an order of magnitude lower during flow through feldspar-rich sandstone (Tutolo et al., 2015).

With the relatively high Fe and Mg concentration and relatively low Ca concentrations, Fe and Mg accounted for most of the divalent metal flux. Outside of the first sample taken for each experiment, Ca concentration accounted for 2-12% of the total concentration of the major divalent metals. Previous work by Gudbrandsson et al. (2011) demonstrated that Fe and Mg release dominate crystalline basalt dissolution at low pH, whereas the relative fraction of Ca release grows as pH increases. Gudbrandsson et al. (2011) noted that this results because dissolution rates of olivine and pyroxene decrease monotonically with pH, whereas dissolution rates for plagioclase initially decrease and then increase as a function of pH. The first sample

collected during all four experiments had a Ca concentration that ranged from 1.9-2.7 mmol/kg (corrected for dilution), indicating that at least a minor part of the plagioclase was characterized by an initially high reactive surface area. Outside of these relatively high, initial concentrations, lower Ca concentrations persisted throughout the rest of the experiments, indicating that plagioclase dissolution contributed relatively little to total core dissolution, even though plagioclase was by far the dominant phase in the rock. Because of this, the experimental fluids reported here are characterized by higher saturation indices for the Fe and Mg carbonates (siderite and magnesite) and lower values for Ca carbonates (dolomite and calcite). Rogers et al. (2006) noted the production of Fe and Mg carbonates arising from basalt interaction with CO₂-rich fluids. In addition, Rosenbauer et al. (2012) reported formation of ferroan magnesite during reaction between basalt and CO₂-acidified brine. Conversely, alteration of oceanic crust produces carbonates that are rich in Ca (Alt et al., 2010; Alt and Teagle, 1999; Coogan and Gillis, 2013; Gillis and Coogan, 2011), which is likely an artifact of the increased rate of plagioclase dissolution at higher pH. Gysi and Stefansson (2012a) noted rapid formation of Ca, Mg, and Fe carbonates at elevated CO₂ and pH < 6.5 at a temperature of 40°C; higher pH resulted in supersaturation with respect to Ca carbonate alone. Schaef et al. (2010, 2011, 2013) identified carbonates containing Ca, Fe, Mg, and Mn after reacting several different basalts with CO₂ and CO₂-H₂S-H₂O solutions. Olsson et al. (2012) identified magnesite, magnesian calcite, and hydromagnesite while reacting CO₂, pure water, and basalt at 120°C.

Even with the precipitation of the Fe₂O₃-rich phase, aqueous Fe was still high enough that siderite was generally saturated or supersaturated during all four experiments, yielding log Ω values up to ~1. Dawsonite was generally near saturation, but Benezeth et al. (2007) noted that dawsonite optimally forms in alkaline environments. Furthermore, Kaszuba et al. (2011)

demonstrated challenges in the prediction of dawsonite formation. Magnesite, dolomite, and calcite were generally undersaturated throughout all four experiments, in part because of the initial composition of the experimental fluid (i.e., negligible alkalinity). However, the saturation index for all four of these carbonates increased with residence time, as can be seen by the increase in saturation values for Experiments 3 and 4 when compared to Experiments 1 and 2. Given more reaction time, saturation indices for these carbonates would continue to rise with additional dissolution. Once nucleation begins, basalt could potentially undergo significant carbonation.

The primary carbonate phases that ultimately form from CO₂-H₂O-basalt interaction are likely dependent on the initial condition and probably change as the system evolves due to fluid-rock reaction. With the CarbFix project in Iceland, CO₂ is injected as a dissolved component in water, with an expected pH of 3-4 near the injection well (Gislason et al., 2014; Sigfusson et al., 2015). We anticipate that this acidic fluid would cause significant leaching of Fe and Mg from the basalt as demonstrated by Gudbrandsson et al. (2011) and confirmed by our experiments, and thus, we would expect precipitation of Fe and Mg carbonates (so long as the Fe is not consumed by iron oxide mineralization) during initial stages of alteration. As the fluid evolves and moves away from the injection well, we anticipate that Ca-rich carbonates would begin to form while precipitation of Fe and Mg carbonates becomes less significant. Eventually, Ca carbonates likely become predominant as the relative importance of plagioclase dissolution increases. In fact, Matter et al. (2016) identified calcite formation on the submersible pump installed in a monitoring well at the CarbFix site, where pH in the well ranged from ~6.6 to ~9.0.

While the susceptibility measurements may suggest possible formation of an Fe-bearing paramagnetic secondary phase during the lower flow rate experiments (3 and 4), Fe was indeed

incorporated into an Fe_2O_3 -rich phase at the very downstream end of the cores from these experiments. Previous research has also noted formation of noncarbonate iron-rich secondary minerals during reaction between basalt and CO_2 -rich fluids. During reaction between olivine and pure water and CO_2 at 120°C , Olsson et al. (2012) used XRD and XPS to identify secondary formation of hematite, in addition to magnesite, magnesian calcite, and hydromagnesite. They also observed hematite formation in an additional experiment specifically conducted in the absence of oxygen. When reacting basalt with CO_2 - H_2S aqueous solutions at 60°C , Schaef et al. (2010) identified iron sulfide (pyrite and marcasite) mineralization. Reaction path modeling at 60°C and 100 bar predicts goethite precipitation during CO_2 sequestration in Columbia River tholeiitic flood basalt (with modeled composition consisting of plagioclase, clinopyroxene, orthopyroxene, and magnetite, but no olivine), although six other secondary minerals (including four carbonates) ultimately exceed goethite formation on a mole basis (Marini 2006). As either iron oxide or iron sulfide formation ultimately limit iron carbonation, research that identifies factors contributing to or inhibiting noncarbonate iron-rich mineral formation provides practical implications for carbon sequestration efforts.

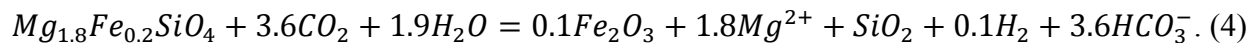
Outlet fluids generally contained dissolved Si that was near saturation with respect to both quartz and amorphous silica. Since thin section analysis revealed a fully crystalline sample, the dissolved Si resulted from the dissolution of silicates. The relatively low Al concentrations in outlet fluids throughout all experiments indicates that most of the Al is retained in the core, due to either stabilization in primary phases that underwent little dissolution or incorporation into secondary minerals. Based on mass balance constraints and outlet fluid chemistry, less than 0.02 wt% of the total Al in the basalt cores was recovered in the outlet fluids. Saturation calculations

suggest that there is a thermodynamic drive to retain Al in a variety of potential Al-rich secondary phases (Figure 5).

Common secondary minerals from basalt alteration include phyllosilicates, zeolites, chalcedony, quartz, and calcite (Alt et al., 2010; Ehlmann et al., 2012; Mehegan et al., 1982; Neuhoﬀ et al., 1999, 2006; Rogers et al., 2006; Seyfried and Bischoﬀ, 1979; Weisenberger and Selbekk, 2009). Major alteration minerals arising from basalt dissolution in the CO₂ injection interval at the CarbFix site in Iceland include Ca-Mg-Fe-smectite, Ca-rich zeolites, and calcite (Alfredsson et al., 2013). The extent of mineral carbonation that can ultimately occur in a basalt reservoir will ultimately be dependent on the Al-rich secondary phase that forms. Smectites, for example, would consume cations dissolved from the rock that would otherwise be available for carbonate formation. However, whereas significant Ca, Mg, and Fe are incorporated into clays in systems with low CO₂, the fraction of Ca, Mg, and Fe going into carbonates will increase with higher CO₂ concentrations (Gysi and Stefánsson, 2011), although Mg and Fe are more eﬀectively incorporated into carbonates at lower temperatures (Gysi and Stefánsson, 2012b, 2012c). Rogers et al. (2006) observed this in West Greenland, where magnesite-siderite solid solutions replaced secondary mafic phyllosilicates and zeolites due to interaction between CO₂-rich fluid associated with petroleum migration and basalt and low-grade metamorphic secondary phases. The carbonates formed between 80 and 126°C (Stannius, 1998).

Experimental parameters provide some constraint on the redox conditions during the experiments. Based on the presence of the Fe₂O₃-rich secondary phase (one example is hematite) and elevated CO₂ with a log activity of -0.16, the log activity of aqueous H₂ could have been up to -8.8 if any siderite formed to buffer the system (Figure 9). That hematite can precipitate in a reducing environment at first seems like a paradox (Evans et al., 2013) since

oxidation is involved as olivine is converted to hematite. However, the oxidation that occurs during this reaction does not require molecular O₂. Instead, water oxidizes the olivine to produce hematite and H₂ via the following reaction



From a mineral carbonation perspective, it is important to note that the presence of hematite does not preclude the formation of siderite. In fact, Figure 9 demonstrates that hematite and siderite can coexist at moderately reducing conditions in CO₂-rich systems. It is also possible that H₂ may have been even higher, since siderite was saturated or supersaturated during our experiments. However, it is problematic to constrain the maximum aqueous H₂ activity given the difficulty of determining if siderite precipitated during the experiments and the inherent uncertainty in saturation calculations.

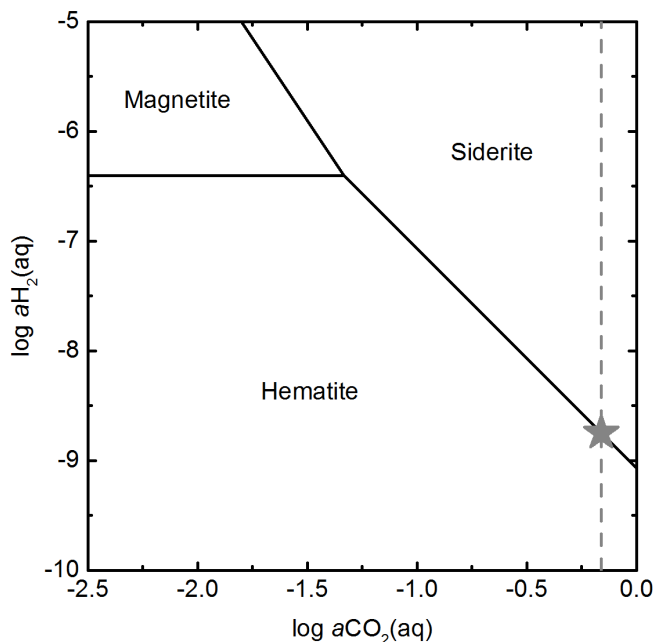


Figure 9. Activity-activity diagram for the FeO-Fe₂O₃-CO₂ system calculated at 150°C.

The gray dashed line illustrates the approximate log aCO₂(aq) from the experiments, and

the gray star constrains the log $a_{\text{H}_2(\text{aq})}$ at -8.8 if hematite and siderite were both present in the core.

Storage of CO_2 in the subsurface will mobilize trace elements and potentially impair water quality (Aiuppa et al., 2000; Galeczka et al., 2013, 2014; Karamalidis et al., 2012; Kirsch et al., 2014; Navarre-Sitchler et al., 2013; Shao et al., 2014; Siirila et al., 2012; Tutolo et al., 2015; Wunsch et al., 2013, 2014). Comparing the outlet fluids to water quality standards (Table 8, USEPA 2012) provides some indication of the degree of metal mobilization during our experiments. Most of the fluid samples collected from the experiments were above the Maximum Contaminant Level (MCL) for Pb, and about half of the samples were above the MCL for Sb. Ba, Cu, As, Cd were initially above the MCL at the beginning of the experiments, but then decreased below this threshold with reaction progress. All samples were below the MCL for Cr and U. Fe and Mn were well above Secondary Drinking Water Regulations (SDWR). Dissolved Al was also above the SDWR for many samples, and there were a couple samples that surpassed the SDWR limit for Zn. It is likely that these metal concentrations are likely a worst-case water quality scenario during CO_2 injection into basalt reservoirs given the nearly saturated CO_2 -charged brine and elevated temperature of our experiments. Furthermore, our experiments simulate a subsurface brine, so any impacts to potable waters would occur during leakage into overlying aquifers, in which case the metal-laden brine would be diluted. Finally, toxic metals from CO_2 -water-rock dissolution are readily incorporated into secondary mineral phases (Flaathen et al., 2009; Olsson et al., 2014; Wigley et al., 2013).

Table 8. US EPA drinking water standards and maximum concentrations from experiments.

Element	Regulatory limit $\mu\text{mol/L}$	Max. conc. from expts. $\mu\text{mol/L}$
Maximum Level (MCL) ^a	Contaminant	
As	0.133	0.300

Ba	14.6	115
Cd	0.0445	0.070
Cr	1.92	1.24
Cu	20.5	123
Pb	0.0724	0.370
Sb	0.0493	0.140
U	0.126	0.0018
Secondary Drinking Water Regulation (SDWR) ^b		
Al	1.85-7.41	64
Fe	5.37	2500
Mn	0.910	97
Zn	76.5	31

^aEnforceable standard.

^bNon-enforceable guideline.

4.2. Reaction modeling of basalt alteration over longer timescales

To assess mass transfer and alteration over longer reaction timescales in more of a transport-limited regime, we have run simulations of fluid-basalt interaction at 150°C using Geochemist's Workbench (Bethke and Yeakel, 2015). 1 kg of water was reacted with 1 kg of rock, consisting of 550 g of labradorite, 290 g of enstatite, 100 g of forsterite, and 60 g of fayalite. We use An50 for our labradorite composition based on the normative mineralogy calculation. While we don't model the olivine solid solution explicitly, we use the Fo70 (composition from the EDS spot analysis on the olivine crystal shown in Figure 6a) composition to determine the relative mass of forsterite and fayalite that is included in the model. A BET surface area of 2,508 cm²/g was measured on a basalt core (Luhmann et al., in review), and this surface area was used for all mineral phases. The water contained 900 mmol/kg of both Na⁺ and Cl⁻ and 100 mmol/kg of HCO₃⁻. Concentrations of other aqueous species were set to 1 µmol/kg. Simulations were run at relatively low and high pH (4 and 9, respectively) to identify the control of pH on element mobility and secondary phase composition. The low pH simulation characterizes CO₂-rich scenarios, and the high pH simulation represents CO₂-poor environments

(e.g., Gíslason and Arnórsson, 1993). pH was fixed in both simulation, and Cl^- and Na^+ concentrations were adjusted to satisfy charge balance constraints in the low pH simulation and the high pH simulation, respectively. Owing to the uncertainties in mineral solid solution effects and mineral surface areas, the calculations necessarily provide information that may capture the relative time series changes in mineral dissolution processes, but is limited in an absolute sense. Only with additional studies of this type, especially with integration of information of mineral alteration processes on the pore scale, can more robust models of mass transfer in time and space be developed.

The simulations employed kinetic dissolution data from the literature. Both forsterite and fayalite were modeled using the dissolution rate law compilation from Rimstidt et al. (2012). The dissolution rate r is given by

$$r = A \exp(-E_a / RT) a_{H^+}^n, \quad (5)$$

where A is the pre-exponential factor, E_a is the activation energy, R is the gas constant, T is temperature, a_i is the activity of species i , and the exponent n is the reaction order of species i . For the low pH simulation, $A = 14.7 \text{ mol/cm}^2/\text{s}$, $E_a = 70,400 \text{ J/mol}$, and $n = 0.44$. For the high pH simulation, $A = 0.0217 \text{ mol/cm}^2/\text{s}$, $E_a = 60,900 \text{ J/mol}$, and $n = 0.22$. Dissolution of enstatite was modeled using the kinetic rate equation from Oelkers and Schott (2001):

$$r = A \exp(-E_a / RT) (a_{H^+}^2 / a_{Mg^{2+}})^{1/8}, \quad (6)$$

where $A = 2.4 \times 10^{-4} \text{ mol/cm}^2/\text{s}$ and $E_a = 48,500 \text{ J/mol}$. Finally, dissolution of labradorite employed the kinetic rate equation of Carroll and Knauss (2005):

$$r = k \exp(-E_a / RT) [(a_{H^+}^{0.93} / a_{Al^{3+}}^{0.31}) K_T / (1 + K_T (a_{H^+}^{0.93} / a_{Al^{3+}}^{0.31}))], \quad (7)$$

where k is the apparent dissolution rate constant ($10^{-5.69}$ mol/cm²/s), $E_a = 42,091$ J/mol, and we extrapolate K_T to be ~ 5.81 at 150°C (Carroll and Knauss (2005) provide K_T for 30 - 130°C).

Multiplying the right side of Equations (5), (6), and (7) by A_m and $(1-(Q/K)^\mu)^\lambda$, where A_m is the surface area and μ and λ are empirically determined parameters, yields units of mol/s for r . In the labradorite dissolution rate equation, the values of μ and λ were set to 0.76 and 90, respectively (determined from albite dissolution by Alekseyev et al. (1997)). The values of μ and λ have not been quantified for forsterite, fayalite, and enstatite, and so we simply use values of unity for both parameters, as is often done (Daval et al., 2009, 2010, 2011; Knauss et al., 2005; Xu et al., 2004). Because labradorite was so far from equilibrium, simply setting μ and λ to unity would cause little change, in which case it would have taken 1.0 days instead of 1.1 days to reduce the amount of labradorite from 2.0 to 0.01 moles in the pH = 4 simulation.

pH provides a strong control on the rate of primary mineral dissolution as well as the composition of the fluid chemistry and precipitated secondary phases (Figure 10). At pH = 4, olivine quickly dissolves and both forsterite and fayalite fall below 0.01 moles within 0.3 days (Figure 10a). Labradorite also dissolves relatively quickly, decreasing to less than 0.01 moles within 1.1 days. Kinetics of enstatite dissolution are slower, but the amount of enstatite decreases by more than an order of magnitude over the five-day simulation. Dissolution of the basalt yields abundant dissolved Mg²⁺ in solution, attaining a concentration of more than 2.4 mol/kg at the end of five days (Figure 10b). Dissolved Fe²⁺ also quickly increases in solution, but is subsequently surpassed by Ca²⁺ because of fayalite consumption and siderite precipitation as well as dissolution of labradorite.

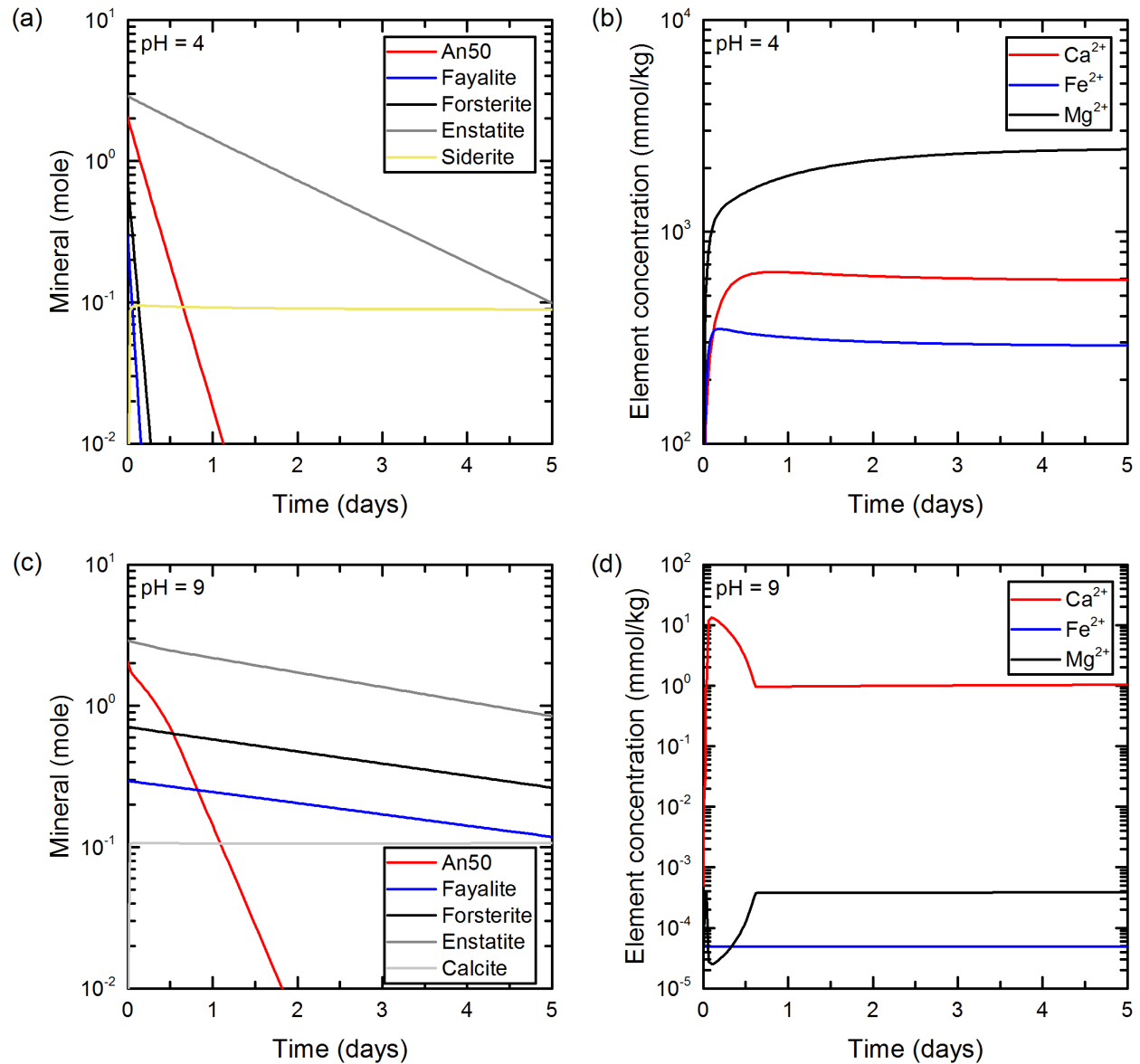


Figure 10. Reaction path models illustrating mass transfer during basalt alteration. (a) At relatively low pH (pH = 4), forsterite and fayalite quickly dissolve and siderite precipitates, (b) while dissolved Mg^{2+} increases significantly. (c) At relatively high pH (pH = 9), labradorite preferentially dissolves and calcite precipitates, (d) even while Ca^{2+} is the most abundant divalent cation in solution. Minerals provided in (a) and (c) only include the modeled basalt composition and secondary carbonates.

At pH = 9, the dissolution rate decreases for labradorite, olivine, and enstatite, but the decrease is much more significant for olivine and enstatite than it is for labradorite (Figure 10c). At the end of the five-day simulation, fayalite, forsterite, and enstatite decrease to 40%, 37%, and 29% of their initial masses, respectively. In contrast, the labradorite decreases to less than 0.01 moles at 1.8 days, which is only 0.7 days longer than the pH = 4 simulation. The concentrations of Ca^{2+} , Fe^{2+} , and Mg^{2+} are much lower in this higher pH simulation, but the Ca^{2+} concentration is now higher than the dissolved Fe^{2+} and Mg^{2+} , even though calcite precipitates due to basalt alteration at higher pH (Figure 10d).

It is interesting to note that the siderite is still the only carbonate phase predicted to form if the initial concentration of Ca^{2+} is increased to 1 mol/kg in the low pH simulation. Furthermore, if the initial concentration of both Ca^{2+} and HCO_3^- are increased to 1 mol/kg in the low pH simulation, the model predicts the production of more than 0.5 moles of siderite and 0.3 moles of dolomite at the end of five days. Because Mg^{2+} is produced so quickly during olivine dissolution at relatively low pH, Ca^{2+} is not consumed by carbonate precipitation as a pure calcium carbonate phase. These simulations do not include kinetics of carbonate precipitation, but at least the thermodynamic data suggest that secondary carbonates contain Fe^{2+} and Mg^{2+} under acidic conditions due to dissolution of olivine. Marini (2006) also showed Fe- and Mg-rich secondary carbonates during CO_2 -water-basalt reaction path modeling under acidic conditions. At a temperature of 60°C and pH ~ 5, Marini (2006) calculated early carbonate formation including dolomite and siderite (after twelve and fifteen months, respectively), and this was eventually followed by precipitation of calcite and dawsonite over longer reaction timescales (8.4 years and 53.4 years, respectively). Gysi and Stefánsson (2012b) also ran models (reacting CO_2 -water-basaltic glass) and noted formation of ankerite, dolomite, Ca-Mg-Fe

carbonate solid solutions, chalcedony, and allophane at 75°C and pH~4.5. Clay mineral formation consumed available Mg and Fe in their models at higher temperatures (150°C and 250°C) at pH of ~5.5 to >6, resulting in calcite as the only forming carbonate phase (Gysi and Stefánsson 2012b). During additional models at 25-90°C, they also noted that Ca, Mg, and Fe were incorporated into carbonates (with Fe serving an important role in CO₂ mineralization) in acidic solutions (pH < 6.5), whereas calcite was the only carbonate to form when pH was greater than 8 (Gysi and Stefánsson 2011).

4.3. Preferential dissolution

Fluids preferentially dissolved alkali metals from the basalt cores (Fig. 11). Element extraction (wt%) is calculated using

$$El\ recovery = \frac{M_i Q_m \int_{t'=0}^{t'=t} \Delta C_i(t') dt'}{m_{core} F_i} \times 100, \quad (8)$$

where M_i is the molecular mass of element i , Q_m is the mass fluid flow rate, ΔC_i is the outlet concentration of element i , t is time, m_{core} is the mass of the core, and F_i is the element weight fraction in the basalt. Only two experiments (one at each flow rate) were analyzed for trace elements with the ICP-MS, but there is generally good reproducibility in the dissolved aqueous chemistry among experiments at a given flow rate, as is shown in the K extraction in Figure 11. Experimental fluid dissolved 13%, 18%, and 9% of the Li, K, and Rb, respectively, from the basalt core by the end of Experiment 3, while the core lost only 1.6% of its initial mass during the course of the experiment (Table 3). At an extreme, the Cs was completely extracted from the core during the course of the experiment (Fig. 11).

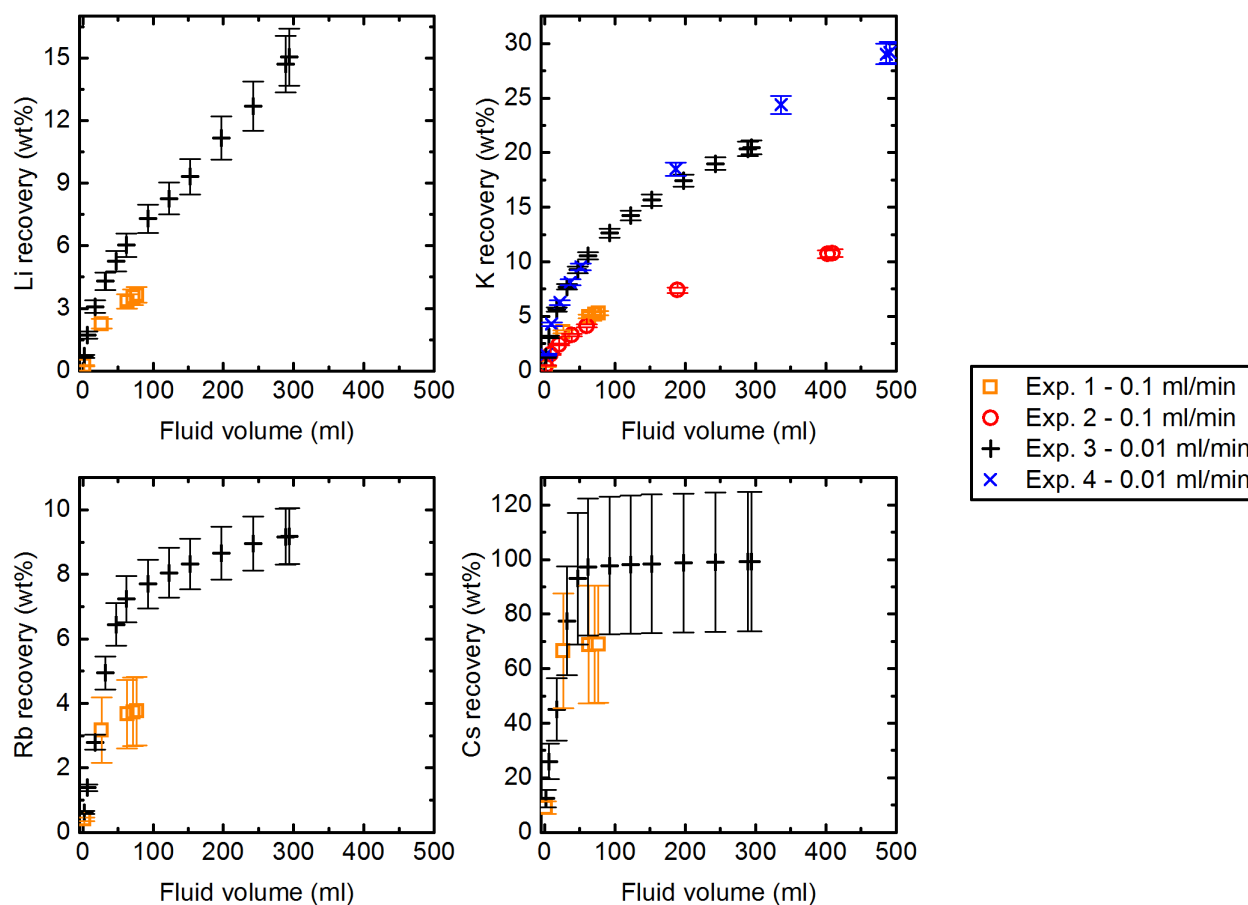


Figure 11. Alkali metals were preferentially dissolved from the basalt cores during fluid-rock interaction, to the extent of complete Cs removal during Experiment 3. While dissolution of major elements is ultimately controlled by solubility constraints, minor elements can be completely removed from a system so long as fluids are able to access these components in the mineral structure, as is evidenced by the highly reactive alkali elements.

Release of alkali metals has been noted in previous experimental work. Seyfried et al. (1984) reported Li leaching from basalt at 375°C and Li removal from fluid during incorporation into smectite at 150°C. Berger et al. (1988) found that Rb and Cs are preferentially released during the dissolution of basalt glass, whereas release of Li is stoichiometric with respect to Si. In contrast, dissolution of forsterite caused preferential release of Li with respect to Si (Berger et al. 1988). Brant et al. (2012) demonstrated that Ba, Rb, Cs, and Li are leached rapidly from

synthetic basalts at 125°C, and ultimately concluded that Li release is primarily controlled by diffusion from plagioclase since crystalline material caused much more Li leaching than glass. However, it is more likely that the preferential dissolution of Li as well as the other alkali metals in the experiments reported here arise from fractional crystallization effects inherent to the initial rock formation. Li, K, Rb, and Cs are highly incompatible in minerals as they crystallize. Furthermore, the absence of glass from the basalt suggests slow cooling, which allows strong chemical gradients to develop across individual mineral grains. Thus, these elements are likely primarily incorporated into outer portions of mineral grains, and therefore, are readily accessible during initial stages of basalt dissolution. Furthermore, it is possible that there are microcracks at the grain scale that allow fluids to more efficiently access and dissolve these incompatible elements (see Luhmann et al. (in review) for a discussion of basalt porosity and surface area over length scales that range from ~1 nm to 10 µm from (U)SANS analyses).

The K dissolution probably arises from dissolution of the plagioclase, where individual grains likely contain a Ca-rich core that progressively becomes more Na- and K-rich toward the outer edges (Figure 6c; Singer et al., 1995). Thus, while the relatively low Ca concentrations suggest little dissolution of plagioclase (at least the Ca-rich component of it), the high K recoveries (up to ~30% of the K from the rock core during Experiment 4) indicate significant dissolution of the plagioclase rich in K. The elevated Rb also likely arises from dissolution of K-rich plagioclase, where Rb potentially substitutes for K in the feldspar structure because of the similar atomic radii of these two elements. Similarly, Li likely substitutes for Mg in the olivine structure because of similar atomic radii, and thus, dissolution of Li arises from dissolution of the outer portions of olivine grains. The minor component of any solid solution is often attributed to

have an activity greater than one, which provides a strong thermodynamic drive for these alkali metals and other minor constituents to enter solution.

The high extraction of these alkali elements illustrates the lack of solubility control for these particular elements, especially for Li, Rb, and Cs. Because of their incompatible nature, there is a strong drive for the alkali metals to enter the fluid, which causes a decrease in slope of the extraction curves with reaction progress as the elements are depleted in the rock, especially for K, Rb, and Cs (Figure 11). Furthermore, extractions are inversely related to flow rate, as also noted in Luhmann et al. (2014). Experiments at the lower flow rate had longer residence time for fluid-rock reaction, and therefore, greater dissolution of the alkali metals from the experimental cores.

5. Conclusions and broader implications

Four flow-through experiments at 150°C were conducted on intact basalt cores to identify chemical processes and changes that arise from basalt-water-CO₂ interaction. See Luhmann et al. (in review) for a discussion of physical property changes in the experiments. Reaction between flowing CO₂-charged brine and basalt produced elevated concentrations of Fe, Mg, and Si in solution. The low pH of our experimental solution (initial pH of 3.3) caused significant basalt dissolution. SEM pictures revealed secondary mineralization on primary minerals of the basalt cores, and fluid saturation calculations suggest kaolinite, analcime, diaspore, K-feldspar, gibbsite, and siderite as potential secondary phases. Both experiments at the higher flow rate of 0.1 ml/min (Experiments 1 and 2) produced permeability increases from fluid-rock reaction, although there was a significant difference in the increase between the two experiments because of the different pre-existing flow paths that were present in the cores. There was a net small

decrease in permeability for both experiments at the lower flow rate of 0.01 ml/min (Experiments 3 and 4), although permeability increased at the end of the experiments following initial decreases. The lower flow rate experiments had more fluid residence time, transitioning from a more dissolution-dominated regime during Experiments 1 and 2 to a regime that facilitates the formation of secondary phases during Experiments 3 and 4.

Our experiments illustrate incipient reaction between basalt and acidic fluids, with implications for fluid-rock reactions in volcanic reservoirs. CO₂ can accumulate in subsurface formations from both natural and anthropogenic sources, as evidenced by ongoing CO₂-injection projects in Iceland and Washington (Gislason et al., 2010; Matter et al., 2009, 2011; McGrail et al., 2011) as well as a number of geothermal systems with elevated CO₂ (Federico et al., 2002, 2004; Flaathen et al., 2009; Fridriksson et al., 2006; Kerrick, 2001; Mörner and Etiope, 2002; Watson et al., 2004). As an extreme, Lupton et al. (2006) report CO₂ concentrations up to 2.7 mol/kg from a submarine volcano in the Mariana Arc, where CO₂ naturally exists as a liquid. In any of these environments, the CO₂ will acidify fluids and react with basalt to produce fluids that have higher saturation indices for Fe and Mg carbonates than carbonates rich in Ca. While experiments presented here represent limited time for fluid-rock reaction, significant precipitation of Fe and Mg carbonates would likely follow given more reaction time, as suggested by our reaction path models and those of Marini (2006) and Gysi and Stefánsson (2011, 2012b) and as demonstrated by observations in West Greenland over longer geologic time (Rogers et al., 2006). However, solution pH would continue to increase with additional fluid-rock reaction, where dissolution of Ca-rich plagioclase would ultimately lead to precipitation of Ca carbonates becoming more significant, as evidenced by formation of calcite at the CarbFix site with fluid pH of ~6.6 – 9.0 (Matter et al. 2016) and during alteration of oceanic crust at

higher pH with little to no dissolved CO₂ (Alt et al., 2010; Alt and Teagle, 1999; Coogan and Gillis, 2013; Gillis and Coogan, 2011). Solution pH is a function of dissolved CO₂, and therefore, the presence or absence of CO₂ exerts a strong control on the secondary mineral carbonate composition during basalt alteration. Because of the strong pH control on the dissolution of the primary mineral phases, pH determines the concentration of divalent metal cations in solution during basalt dissolution, and coincidentally, controls what cations are available to form secondary carbonates. Therefore, analysis of secondary carbonate composition from the rock record can potentially be used to infer environmental conditions during their formation.

Acknowledgements

We thank Travis McLing from the Idaho National Laboratory for providing the basalt borehole sample, Rick Knurr for fluid and rock analyses, Nick Seaton for SEM pictures and analyses, and Anette von der Handt for the electron microprobe analyses. The SEM image in Figure 7a was collected at LacCore, University of Minnesota. SEM images in Figure 6 were taken in the Characterization Facility, University of Minnesota, a member of the NSF-funded Materials Research Facilities Network (www.mrfn.org) via the MRSEC program. The Institute for Rock Magnetism is supported by grants from the Instruments and Facilities Program, Division of Earth Science, National Science Foundation. Research support was provided by the Initiative for Renewable Energy and the Environment (IREE), a signature program of the Institute on the Environment at UMN, the US Department of Energy (DOE) Geothermal Technologies Program through Grant DE-EE0002764, and the National Science Foundation through Grant OCE 1426695. M.O.S. also thanks the George and Orpha Gibson Endowment for its support of the Hydrogeology and Geofluids Research Group at the University of Minnesota

and the Werner Siemens Stiftung/Endowment for its support of the Geothermal Energy and Geofluids Group at ETH-Zurich, Switzerland.

References

- Ackerman, D.J., 1991. Transmissivity of the Snake River Plain Aquifer at the Idaho National Engineering Laboratory, Idaho. U.S. Department of the Interior, U.S. Geological Survey, Water-Resources Investigations Report 91-4058, Idaho Falls, ID, 35p.
- Aiuppa, A., Allard, P., D'Alessandro, W., Michel, A., Parello, F., Treuil, M., Valenza, M., 2000. Mobility and fluxes of major, minor and trace metals during basalt weathering and groundwater transport at Mt. Etna volcano (Sicily). *Geochim. Cosmochim. Acta* 64 (11), 1827-1841.
- Alekseyev, V.A., Medvedeva, L.S., Prisyagina, N.I., Meshalkin, S.S., Balabin, A.I., 1997. Change in the dissolution rates of alkali feldspars as a result of secondary mineral precipitation and approach to equilibrium. *Geochim. Cosmochim. Acta* 61 (6), 1125-1142.
- Alfredsson, H.A., Oelkers, E.H., Hardarsson, B.S., Franzson, H., Gunnlaugsson, E., Gislason, S.R., 2013. The geology and water chemistry of the Hellisheidi, SW-Iceland carbon storage site. *Int. J. Greenh. Gas Control* 12, 399-418.
- Alt, J.C., Teagle, D.A.H., 1999. The uptake of carbon during alteration of ocean crust. *Geochim. Cosmochim. Acta* 63 (10), 1527-1535.
- Alt, J.C., Laverne, C., Coggon, R.M., Teagle, D.A.H., Banerjee, N.R., Morgan, S., Smith-Duque, C.E., Harris, M., Galli, L., 2010. Subsurface structure of a submarine hydrothermal system in ocean crust formed at the East Pacific Rise, ODP/IODP Site 1256. *Geochem. Geophys. Geosy.* 11 (10), Q10010, doi:10.1029/2010GC003144.
- Andreani, M., Luquot, L., Gouze, P., Godard, M., Hoisé, E., Gibert, B., 2009. Experimental study of carbon sequestration reactions controlled by the percolation of CO₂-rich brine through peridotites. *Environ. Sci. Technol.* 43 (4), 1226-1231.
- Arnórsson, S., Stefánsson, A., 1999. Assessment of feldspar solubility constants in water in the range 0° to 350°C at vapor saturation pressures. *Am. J. Sci.* 299, 173-209.
- Bénézech, P., Palmer, D.A., Anovitz, L.M., Horita, J., 2007. Dawsonite synthesis and reevaluation of its thermodynamic properties from solubility measurements: Implications for mineral trapping of CO₂. *Geochim. Cosmochim. Acta* 71 (18), 4438-4455, doi:10.1016/j.gca.2007.07.003.
- Berger, G., Schott, J., Guy, C., 1988. Behavior of Li, Rb and Cs during basalt glass and olivine dissolution and chlorite, smectite and zeolite precipitation from seawater: Experimental investigations and modelization between 50° and 300°C. *Chem. Geol.* 71 (4), 297-312.
- Bethke, C.M., Yeakel, S., 2015. The Geochemist's Workbench® Release 10.0 Reaction Modeling Guide. Aqueous Solutions, LLC, Champaign, IL.
- Brant, C., Coogan, L.A., Gillis, K.M., Seyfried, Jr., W.E., Pester, N.J., Spence, J., 2012. Lithium and Li-isotopes in young altered upper oceanic crust from the East Pacific Rise. *Geochim. Cosmochim. Acta* 96, 272-293, doi:10.1016/j.gca.2012.08.025.
- Carroll, S.A., Knauss, K.G., 2005. Dependence of labradorite dissolution kinetics on CO_{2(aq)}, Al_(aq), and temperature. *Chem. Geol.* 217 (3-4), 213-225.

- Chen, Y., Brantley, S.L., 1998. Diopside and anthophyllite dissolution at 25° and 90°C and acid pH. *Chem. Geol.* 147 (3-4), 233-248.
- Chen, Y., Brantley, S.L., 2000. Dissolution of forsteritic olivine at 65°C and $2 < \text{pH} < 5$. *Chem. Geol.* 165 (3-4), 267-281.
- Chou, L., Wollast, R., 1985. Steady-state kinetics and dissolution mechanisms of albite. *Am. J. Sci.* 285 (10), 963-993.
- Coogan, L.A., Gillis, K.M., 2013. Evidence that low-temperature oceanic hydrothermal systems play an important role in the silicate-carbonate weathering cycle and long-term climate regulation. *Geochim. Geophys. Geosy.* 14 (6), 1771-1786, doi:10.1002/ggge.20113.
- Daval, D., Martinez, I., Corvisier, J., Findling, N., Goffé, B., Guyot, F., 2009. Carbonation of Ca-bearing silicates, the case of wollastonite: Experimental investigations and kinetic modeling. *Chem. Geol.* 265 (1-2), 63-78.
- Daval, D., Testemale, D., Recham, N., Tarascon, J.-M., Siebert, J., Martinez, I., Guyot, F., 2010. Fayalite (Fe_2SiO_4) dissolution kinetics determined by X-ray absorption spectroscopy. *Chem. Geol.* 275 (3-4), 161-175.
- Daval, D., Sissmann, O., Menguy, N., Saldi, G.D., Guyot, F., Martinez, I., Corvisier, J., Garcia, B., Machouk, I., Knauss, K.G., Hellmann, R., 2011. Influence of amorphous silica layer formation on the dissolution rate of olivine at 90 °C and elevated $p\text{CO}_2$. *Chem. Geol.* 284 (1-2), 193-209.
- Dessert, C., Dupré, B., Gaillardet, J., François, L.M., Allègre, C.J., 2003. Basalt weathering laws and the impact of basalt weathering on the global carbon cycle. *Chem. Geol.* 202 (3-4), 257-273.
- Duan, Z., Sun, R., 2003. An improved model calculating CO_2 solubility in pure water and aqueous NaCl solutions from 273 to 533 K and from 0 to 2000 bar. *Chem. Geol.* 193 (3-4), 257-271.
- Duan, Z., Sun, R., Zhu, C., Chou, I.-M., 2006. An improved model for the calculation of CO_2 solubility in aqueous solutions containing Na^+ , K^+ , Ca^{2+} , Mg^{2+} , Cl^- , and SO_4^{2-} . *Mar. Chem.* 98 (2-4), 131-139, doi:10.1016/j.marchem.2005.09.001.
- Duan, Z., Hu, J., Li, D., Mao, S., 2008. Densities of the CO_2 - H_2O and CO_2 - H_2O -NaCl systems up to 647 K and 100 MPa. *Energ. Fuel.* 22 (3), 1666-1674.
- Ehlmann, B.L., Bish, D.L., Ruff, S.W., Mustard, J.F., 2012. Mineralogy and chemistry of altered Icelandic basalts: Application to clay mineral detection and understanding aqueous environments on Mars. *J. Geophys. Res.-Planet.* 117, E00J16, doi:10.1029/2012JE004156.
- Evans, B.W., Hattori, K., Baronnet, A., 2013. Serpentinite: What, why, where? *Elements* 9, 99-106.
- Federico, C., Aiuppa, A., Allard, P., Bellomo, S., Jean-Baptiste, P., Parello, F., Valenza, M., 2002. Magma-derived gas influx and water-rock interactions in the volcanic aquifer of Mt. Vesuvius, Italy. *Geochim. Cosmochim. Acta* 66 (6), 963-981.
- Federico, C., Aiuppa, A., Favara, R., Gurrieri, S., Valenza, M., 2004. Geochemical monitoring of groundwaters (1998-2001) at Vesuvius volcano (Italy). *J. Volcanol. Geoth. Res.* 133 (1-4), 81-104, doi:10.1016/S0377-0273(03)00392-5.
- Felmy, A.R., Qafoku, O., Arey, B.W., Hu, J.Z., Hu, M., Schaef, H.T., Ilton, E.S., Hess, N.J., Pearce, C.I., Feng, J., Rosso, K.M., 2012. Reaction of water-saturated supercritical CO_2 with forsterite: Evidence for magnesite formation at low temperatures. *Geochim. Cosmochim. Acta* 91, 271-282, doi:10.1016/j.gca.2012.05.026.

- Ferrante M.J., Stuve J.M. Richardson D.W., 1976. Thermodynamic data for synthetic dawsonite. U.S. Bureau of Mines Report Investigation, 8129, Washington, D.C., 13p.
- Flaathen, T.K., Gislason, S.R., Oelkers, E.H., Sveinbjörnsdóttir, Á.E., 2009. Chemical evolution of the Mt. Hekla, Iceland, groundwaters: A natural analogue for CO₂ sequestration in basaltic rocks. *Appl. Geochem.* 24 (3), 463-474. doi:10.1016/j.apgeochem.2008.12.031.
- Frederichs, T., von Döbeneck, T. Bleil, U. Dekkers, M.J., 2003. Towards the identification of siderite, rhodochrosite, and vivianite in sediments by their low-temperature magnetic properties. *Phys. Chem. Earth* 28 (16-19), 669-679, doi:10.1016/S1474-7065(03)00121-9.
- Fridriksson, T., Kristjánsson, B.R., Ármannsson, H., Margrétardóttir, E., Ólafsdóttir, S., Chiodini, G., 2006. CO₂ emissions and heat flow through soil, fumaroles, and steam heated mud pools at the Reykjanes geothermal area, SW Iceland. *Appl. Geochem.* 21 (9), 1551-1569, doi:10.1016/j.apgeochem.2006.04.006.
- Galeczka, I., Wolff-Boenisch, D., Gislason, S., 2013. Experimental studies of basalt-H₂O-CO₂ interaction with a high pressure column flow reactor: The mobility of metals. *Energy Procedia* 37, 5823-5833, doi: 10.1016/j.egypro.2013.06.505.
- Galeczka, I., Wolff-Boenisch, D., Oelkers, E.H., Gislason, S.R., 2014. An experimental study of basaltic glass-H₂O-CO₂ interaction at 22 and 50 °C: Implications for subsurface storage of CO₂. *Geochim. Cosmochim. Acta* 126, 123-145, doi:10.1016/j.gca.2013.10.044.
- Giammar, D.E., Bruant, Jr., R.G., Peters, C.A., 2005. Forsterite dissolution and magnesite precipitation at conditions relevant for deep saline aquifer storage and sequestration of carbon dioxide. *Chem. Geol.* 217 (3-4), 257-276. doi:10.1016/j.chemgeo.2004.12.013.
- Gillis, K.M., Coogan, L.A., 2011. Secular variation in carbon uptake into the ocean crust. *Earth Planet. Sc. Lett.* 302 (3-4), 385-392, doi:10.1016/j.epsl.2010.12.030.
- Gislason, S.R., Arnórsson, S., 1993. Dissolution of primary basaltic minerals in natural waters: saturation state and kinetics. *Chem. Geol.* 105 (1-3), 117-135.
- Gislason, S.R., Oelkers, E.H., 2003. Mechanism, rates, and consequences of basaltic glass dissolution: II. An experimental study of the dissolution rates of basaltic glass as a function of pH and temperature. *Geochim. Cosmochim. Acta* 67 (20), 3817-3832, doi:10.1016/S0016-7037(00)00176-5.
- Gislason, S.R., Wolff-Boenisch, D., Stefansson, A., Oelkers, E.H., Gunnlaugsson, E., Sigurdardóttir, H., Sigfusson, B., Broecker, W.S., Matter, J.M., Stute, M., Axelsson, G., Fridriksson, T., 2010. Mineral sequestration of carbon dioxide in basalt: A pre-injection overview of the CarbFix project. *Int. J. Greenh. Gas Control* 4 (3), 537-545, doi:10.1016/j.ijggc.2009.11.013.
- Gislason, S.R., Oelkers, E.H., 2014. Carbon storage in basalt. *Science* 344 (6182), 373-374, doi:10.1126/science.1250828.
- Gislason, S.R., Broecker, W.S., Gunnlaugsson, E., Snæbjörnsdóttir, S., Mesfin, K.G., Alfredsson, H.A., Aradóttir, E.S., Sigfusson, B., Gunnarsson, I., Stute, M., Matter, J.M., Arnarson, M.Th., Galeczka, I.M., Gudbrandsson, S., Stockman, G., Wolff-Boenisch, D., Stefansson, A., Ragnheidardóttir, E., Flaathen, T., Gysi, A.P., Olssen, J., Didriksen, K., Stipp, S., Menez, B., Oelkers, E.H., 2014. Rapid solubility and mineral storage of CO₂ in basalt. *Energy Procedia* 63, 4561-4574, doi:10.1016/j.egypro.2014.11.489.
- Goldberg, D.S., Takahashi, T., Slagle, A.L., 2008. Carbon dioxide sequestration in deep-sea basalt. *P. Natl. Acad. Sci.* 105 (29), 9920-9925.

- Goldberg, D., Slagle, A.L., 2009. A global assessment of deep-sea basalt sites for carbon sequestration. *Energy Procedia*, 1 (1), 3675-3682, doi:10.1016/j.egypro.2009.02.165.
- Gudbrandsson, S., Wolff-Boenisch, D., Gislason, S.R., Oelkers, E.H., 2011. An experimental study of crystalline basalt dissolution from $2 \leq \text{pH} \leq 11$ and temperatures from 5 to 75 °C. *Geochim. Cosmochim. Acta* 75 (19), 5496-5509, doi:10.1016/j.gca.2011.06.035.
- Gudbrandsson, S., Wolff-Boenisch, D., Gislason, S.R., Oelkers, E.H., 2014. Experimental determination of plagioclase dissolution rates as a function of its composition and pH at 22 °C. *Geochim. Cosmochim. Acta* 139, 154-172, doi:10.1016/j.gca.2014.04.028.
- Guy, C., Schott, J., 1989. Multisite surface reaction versus transport control during the hydrolysis of a complex oxide. *Chem. Geol.* 78 (3-4), 181-204.
- Gysi, A.P., Stefánsson, A., 2011. CO₂-water-basalt interaction. Numerical simulation of low temperature CO₂ sequestration into basalts. *Geochim. Cosmochim. Acta* 75 (17), 4728-4751, doi:10.1016/j.gca.2011.05.037.
- Gysi, A.P., Stefánsson, A., 2012a. CO₂-water-basalt interaction. Low temperature experiments and implications for CO₂ sequestration into basalts. *Geochim. Cosmochim. Acta* 81, 129-152, doi:10.1016/j.gca.2011.12.012.
- Gysi, A.P., Stefánsson, A., 2012b. Experiments and geochemical modeling of CO₂ sequestration during hydrothermal basalt alteration. *Chem. Geol.* 306-307, 10-28, doi:10.1016/j.chemgeo.2012.02.016.
- Gysi, A.P., Stefánsson, A., 2012c. Mineralogical aspects of CO₂ sequestration during hydrothermal basalt alteration – An experimental study at 75 to 250 °C and elevated *p*CO₂. *Chem. Geol.* 306-307, 146-159, doi:10.1016/j.chemgeo.2012.03.006.
- Hänchen, M., Prigobbe, V., Storti, G., Seward, T.M., Mazzotti, M., 2006. Dissolution kinetics of fosteritic olivine at 90–150 °C including effects of the presence of CO₂. *Geochim. Cosmochim. Acta* 70 (17), 4403-4416, doi:10.1016/j.gca.2006.06.1560.
- Hughes, S.S., McCurry, M., Geist, D.J., 2002. Geochemical correlations and implications for the magmatic evolution of basalt flow groups at the Idaho National Engineering and Environmental Laboratory, *in* Link, P.K., Mink, L.L. (Eds.), *Geology, Hydrogeology, and Environmental Remediation: Idaho National Engineering and Environmental Laboratory, Eastern Snake River Plain, Idaho: Boulder, Colorado, Geological Society of America Special Paper 353*, p. 151-173.
- IPCC, 2005. IPCC Special Report on Carbon Dioxide Capture and Storage. In: Metz, B., Davidson, O., de Coninck, H.C., Loos, M., Meyer, L.A. (Eds.), *Prepared by Working Group III of the Intergovernmental Panel on Climate Change, Cambridge University Press, Cambridge, United Kingdom and New York, NY, USA* (442 pp.).
- Johnson, G.K., Flotow, H.E., O'Hare, P.A.G., Wise, W.S., 1982. Thermodynamic studies of zeolites: analcime and dehydrated analcime. *Am. Mineral.* 67, 736-748.
- Johnson, J.W., Oelkers, E.H., Helgeson, H.C., 1992. SUPCRT92: A software package for calculating the standard molal thermodynamic properties of minerals, gases, aqueous species, and reactions from 1 to 5000 bar and 0 to 1000°C. *Comput. Geosci.* 18 (7), 899-947.
- Johnson, N.C., Thomas, B., Maher, K., Rosenbauer, R.J., Bird, D., Brown, Jr., G.E., 2014. Olivine dissolution and carbonation under conditions relevant for in situ carbon storage. *Chem. Geol.* 373, 93-105, doi:10.1016/j.chemgeo.2014.02.026.

- Karamalidis, A.K., Torres, S.G., Hakala, J.A., Shao, H., Cantrell, K.J., Carroll, S., 2013. Trace metal source terms in carbon sequestration environments. *Environ. Sci. Technol.* 47 (1), 322-329, doi:10.1021/es304832m.
- Kaszuba, J.P., Viswanathan, H.S., Carey, J.W., 2011. Relative stability and significance of dawsonite and aluminum minerals in geologic carbon sequestration. *Geophys. Res. Lett.* 38 (8), L08404, doi:10.1029/2011GL046845.
- Kerrick, D.M., 2001. Present and past nonanthropogenic CO₂ degassing from the solid Earth. *Rev. Geophys.* 39 (4), 565-585.
- Kestin, J., Khalifa, H.E., Correia, R.J., 1981. Tables of the dynamic and kinematic viscosity of aqueous NaCl solutions in the temperature range 20-150°C and the pressure range 0.1-35 MPa. *J. Phys. Chem. Ref. Data* 10 (1), 71-87.
- Kharaka, Y.K., Thordsen, J.J., Hovorka, S.D., Nance, H.S., Cole, D.R., Phelps, T.J., Knauss, K.G., 2009. Potential environmental issues of CO₂ storage in deep saline aquifers: Geochemical results from the Frio-I Brine Pilot test, Texas, USA. *Appl. Geochem.* 24 (6), 1106-1112, doi:10.1016/j.apgeochem.2009.02.010.
- Kirsch, K., Navarre-Sitchler, A.K., Wunsch, A., McCray, J.E., 2014. Metal release from sandstones under experimentally and numerically simulated CO₂ leakage conditions. *Environ. Sci. Technol.* 48 (3), 1436-1442, doi:10.1021/es403077b.
- Knauss, K.G., Wolery, T.J., 1986. Dependence of albite dissolution kinetics on pH and time at 25°C and 70°C. *Geochim. Cosmochim. Acta* 50 (11), 2481-2497.
- Knauss, K.G., Nguyen, S.N., Weed, H.C., 1993. Diopside dissolution kinetics as a function of pH, CO₂, temperature, and time. *Geochim. Cosmochim. Acta* 57 (2), 285-294.
- Knauss, K.G., Johnson, J.W., Steefel, C.I., 2005. Evaluation of the impact of CO₂, co-contaminant gas, aqueous fluid and reservoir rock interactions on the geologic sequestration of CO₂. *Chem. Geol.* 217 (3-4), 339-350.
- Kong, X.-Z., Tutolo, B.M., Saar, M.O., 2013. DBCreate: A SUPCRT92-based program for producing EQ3/6, TOUGHREACT, and GWB thermodynamic databases at user-defined *T* and *P*. *Comput. Geosci.* 51, 415-417, doi:10.1016/j.cageo.2012.08.004.
- Luhmann, A.J., Kong, X.-Z., Tutolo, B.M., Ding, K., Saar, M.O., Seyfried, Jr., W.E., 2013. Permeability reduction produced by grain reorganization and accumulation of exsolved CO₂ during geologic carbon sequestration: A new CO₂ trapping mechanism. *Environ. Sci. Technol.* 47 (1), 242-251, doi:10.1021/es3031209.
- Luhmann, A.J., Kong, X.-Z., Tutolo, B.M., Garapati, N., Bagley, B.C., Saar, M.O., Seyfried, Jr., W.E., 2014. Experimental dissolution of dolomite by CO₂-charged brine at 100 °C and 150 bar: Evolution of porosity, permeability, and reactive surface area. *Chem. Geol.* 380: 145-160, doi:10.1016/j.chemgeo.2014.05.001.
- Luhmann, A.J., Tutolo, B.M., Bagley, B.C., Mildner, D.F.R., Seyfried, Jr., W.E., Saar, M.O., In review. Permeability, porosity, and mineral surface area changes in basalt cores induced by reactive transport of CO₂-rich brine. *Water Resour. Res.*
- Lupton, J., Butterfield, D., Lilley, M., Evans, L., Nakamura, K.I., Chadwick, Jr., W., Resing, J., Embley, R., Olson, E., Proskurowski, G., Baker, E., de Ronde, C., Roe, K., Greene, R., Lebon, G., Young, C. 2006. Submarine venting of liquid carbon dioxide on a Mariana Arc volcano. *Geochem. Geophys. Geosy.* 7 (8), Q08007, doi:10.1029/2005GC001152.
- Luquot, L., Andreani, M., Gouze, P., Camps, P., 2012. CO₂ percolation experiments through chlorite/zeolite-rich sandstone (Pretty Hill Formation – Otway Basin – Australia). *Chem. Geol.* 294-295, 75-88, doi:10.1016/j.chemgeo.2011.11.018.

- Mao, S., Duan, Z., 2009. The viscosity of aqueous alkali-chloride solutions up to 623 K, 1,000 bar, and high ionic strength. *Int. J. Thermophys.* 30, 1510-1523, doi:10.1007/s10765-009-0646-7.
- Marini, L. (2006). *Geological Sequestration of Carbon Dioxide: Thermodynamics, Kinetics, and Reaction Path Modeling*. Developments in Geochemistry 11. Elsevier, Amsterdam.
- Matter, J.M., Takahashi, T., Goldberg, D., 2007. Experimental evaluation of in situ CO₂-water-rock reactions during CO₂ injection in basaltic rocks: Implications for geological CO₂ sequestration. *Geochem. Geophys. Geosy.* 8 (2), Q02001, doi:10.1029/2006GC001427.
- Matter, J.M., Broecker, W.S., Stute, M., Gislason, S.R., Oelkers, E.H., Stefánsson, A., Wolff-Boenisch, D., Gunnlaugsson, E., Axelsson, G., Björnsson, G., 2009. Permanent carbon dioxide storage into basalt: The CarbFix pilot project, Iceland. *Energy Procedia*, 1 (1), 3641-3646, doi:10.1016/j.egypro.2009.02.160.
- Matter, J.M., Kelemen, P.B., 2009. Permanent storage of carbon dioxide in geological reservoirs by mineral carbonation. *Nat. Geosci.* 2, 837-841, doi:10.1038/ngeo683.
- Matter, J.M., Broecker, W.S., Gislason, S.R., Gunnlaugsson, E., Oelkers, E.H., Stute, M., Sigurdardóttir, H., Stefánsson, A., Alfredsson, H.A., Aradóttir, E.S., Axelsson, G., Sigfússon, B., Wolff-Boenisch, D., 2011. The CarbFix pilot project — Storing carbon dioxide in basalt. *Energy Procedia* 4, 5579–5585, doi:10.1016/j.egypro.2011.02.546.
- Matter, J.M., Stute, M., Snæbjörnsdóttir, S.Ó., Oelkers, E.H., Gislason, S.R., Aradóttir, E.S., Sigfússon, B., Gunnarsson, I., Sigurdardóttir, H., Gunnlaugsson, E., Axelsson, G., Alfredsson, H.A., Wolff-Boenisch, D., Mesfin, K., de la Reguera Taya, D.F., Hall, J., Dideriksen, K., Broecker, W.S., 2016. Rapid carbon mineralization for permanent disposal of anthropogenic carbon dioxide emissions. *Science*, 352 (6291), 1312-1314, doi:10.1126/science.aad8132.
- McLing, T.L., 1994. *The Pre-Anthropogenic Groundwater Evolution at the Idaho National Engineering Laboratory, Idaho*. M.Sc. Thesis, Idaho State University, Pocatello, ID.
- McGrail, B.P., Schaef, H.T., Ho, A.M., Chien, Y.-J., Dooley, J.J., Davidson, C.L., 2006. Potential for carbon dioxide sequestration in flood basalts. *J. Geophys. Res.-Sol. Ea.* 111, B12201, doi:10.1029/2005JB004169.
- McGrail, B.P., Spane, F.A., Sullivan, E.C., Bacon, D.H., Hund, G., 2011. The Wallula basalt sequestration pilot project. *Energy Procedia* 4, 5653-5660, doi:10.1016/j.egypro.2011.02.557.
- Mehegan, J.M., Robinson, P.T., Delaney, J.R., 1982. Secondary mineralization and hydrothermal alteration in the Reydarfjörður drill core, eastern Iceland. *J. Geophys. Res.: Solid Earth*, 87 (B8), 6511-6524.
- Mörner, N.-A., Etiope, G., 2002. Carbon degassing from the lithosphere. *Global Planet. Change* 33 (1-2), 185-203.
- NACSA, 2012. *The North American Carbon Storage Atlas*. www.nacsap.org.
- Navarre-Sitchler, A.K., Maxwell, R.M., Siirila, E.R., Hammond, G.E., Lichtner, P.C., 2013. Elucidating geochemical response of shallow heterogeneous aquifers to CO₂ leakage using high-performance computing: Implications for monitoring of CO₂ sequestration. *Adv. Water Resour.* 53, 45-55, doi:10.1016/j.advwatres.2012.10.005.
- Neuhoff, P.S., Fridriksson, T., Arnórsson, S., Bird, D.K., 1999. Porosity evolution and mineral paragenesis during low-grade metamorphism of basaltic lavas at Teigarhorn, eastern Iceland. *Am. J. Sci.* 299, 467-501.

- Neuhoff, P.S., Rogers, K.L., Stannius, L.S., Bird, D.K., Pedersen, A.K., 2006. Regional very low-grade metamorphism of basaltic lavas, Disko–Nuussuaq region, West Greenland. *Lithos* 92 (1-2), 33-54, doi:10.1016/j.lithos.2006.03.028
- Oelkers, E.H., Schott, J., 2001. An experimental study of enstatite dissolution rates as a function of pH, temperature, and aqueous Mg and Si concentration, and the mechanism of pyroxene/pyroxenoid dissolution. *Geochim. Cosmochim. Acta* 65 (8), 1219-1231.
- Oelkers, E.H., Gislason, S.R., Matter, J., 2008. Mineral carbonation of CO₂. *Elements* 4 (5), 333-337, doi:10.2113/gselements.4.5.333.
- Olsson, J., Bovet, N., Makovicky, E., Bechgaard, K., Balogh, Z., Stipp, S.L.S., 2012. Olivine reactivity with CO₂ and H₂O on a microscale: Implications for carbon sequestration. *Geochim. Cosmochim. Acta* 77, 86-97, doi:10.1016/j.gca.2011.11.001.
- Olsson, J., Stipp, S.L.S., Makovicky, E., Gislason, S.R., 2014. Metal scavenging by calcium carbonate at the Eyjafjallajökull volcano: A carbon capture and storage analogue. *Chem. Geol.* 384, 135-148, doi:10.1016/j.chemgeo.2014.06.025.
- Peuble, S., Godard, M., Luquot, L., Andreani, M., Martinez, I., Gouze, P., 2015. CO₂ geological storage in olivine rich basaltic aquifers: New insights from reactive-percolation experiments. *Appl. Geochem.* 52, 174-190, doi:10.1016/j.apgeochem.2014.11.024.
- Pokrovsky, O.S., Schott, J., 2000. Kinetics and mechanism of forsterite dissolution at 25°C and pH from 1 to 12. *Geochim. Cosmochim. Acta* 64 (19), 3313-3325.
- Rimstidt, J.D., Brantley, S.L., Olsen, A.A., 2012. Systematic review of forsterite dissolution rate data. *Geochim. Cosmochim. Acta* 99, 159-178, doi:http://dx.doi.org/10.1016/j.gca.2012.09.019.
- Robie, R.A., Hemingway, B.S., 1995. *Thermodynamic Properties of Minerals and Related Substances at 298.15 K and 1 Bar (10⁵ Pascals) Pressure and at Higher Temperatures*. U.S. Geological Survey Bulletin 2131.
- Rogers, K.L., Neuhoff, P.S., Pedersen, A.K., Bird, D.K., 2006. CO₂ metasomatism in a basalt-hosted petroleum reservoir, Nuussuaq, West Greenland. *Lithos* 92 (1-2), 55-82, doi:10.1016/j.lithos.2006.04.002.
- Rosenbauer, R.J., Thomas, B., Bischoff, J.L., Palandri, J., 2012. Carbon sequestration via reaction with basaltic rocks: Geochemical modeling and experimental results. *Geochim. Cosmochim. Acta* 89, 116-133, doi:10.1016/j.gca.2012.04.042.
- Rosso, J.J., Rimstidt, J.D., 2000. A high resolution study of forsterite dissolution rates. *Geochim. Cosmochim. Acta* 64 (5), 797-811.
- Schaef, H.T., McGrail, B.P., 2009. Dissolution of Columbia River Basalt under mildly acidic conditions as a function of temperature: Experimental results relevant to the geological sequestration of carbon dioxide. *Appl. Geochem.* 24 (5), 980-987, doi:10.1016/j.apgeochem.2009.02.025.
- Schaef, H.T., McGrail, B.P., Owen, A.T., 2010. Carbonate mineralization of volcanic province basalts. *Int. J. Greenh. Gas Control* 4 (2), 249-261, doi:10.1016/j.ijggc.2009.10.009.
- Schaef, H.T., McGrail, B.P., Owen, A.T., 2011. Basalt reactivity variability with reservoir depth in supercritical CO₂ and aqueous phases. *Energy Procedia* 4, 4977-4984, doi:10.1016/j.egypro.2011.02.468.
- Schaef, H.T., McGrail, B.P., Loring, J.L., Bowden, M.E., Arey, B.W., Rosso, K.M., 2012. Forsterite [Mg₂SiO₄] carbonation in wet supercritical CO₂: An in situ high-pressure X-ray diffraction study. *Environ. Sci. Technol.* 47 (1), 174-181, doi:10.1021/es301126f.

- Schaef, H.T., McGrail, B.P., Owen, A.T., Arey, B.W., 2013. Mineralization of basalts in the CO₂–H₂O–H₂S system. *Int. J. Greenh. Gas Control* 16, 187-196, doi:10.1016/j.ijggc.2013.03.020.
- Schaef, H.T., Horner, J.A., Owen, A.T., Thompson, C.J., Loring, J.S., McGrail, B.P., 2014. Mineralization of basalts in the CO₂–H₂O–SO₂–O₂ System. *Environ. Sci. Technol.* 48 (9), 5298-5305, doi:10.1021/es404964j.
- Seyfried, Jr., W.E., Bischoff, J.L., 1979. Low temperature basalt alteration by seawater: An experimental study at 70°C and 150°C. *Geochim. Cosmochim. Acta* 43 (12), 1937-1947.
- Seyfried, Jr., W.E., Janecky, D.R., Mottl, M.J., 1984. Alteration of the oceanic crust: Implications for geochemical cycles of lithium and boron. *Geochim. Cosmochim. Acta* 48 (3), 557-569.
- Shao, H., Kukkadapu, R.K., Krogstad, E.J., Newburn, M.K., Cantrell, K.J., 2014. Mobilization of metals from Eau Claire siltstone and the impact of oxygen under geological carbon dioxide sequestration conditions. *Geochim. Cosmochim. Acta* 141, 62-82, doi:10.1016/j.gca.2014.06.011.
- Sigfusson, B., Gislason, S.R., Matter, J.M., Stute, M., Gunnlaugsson, E., Gunnarsson, I., Aradottir, E.S., Sigurdardottir, H., Mesfin, K., Alfredsson, H.A., Wolff-Boenisch, D., Arnarsson, M.T., Oelkers, E. H., 2015. Solving the carbon-dioxide buoyancy challenge: The design and field testing of a dissolved CO₂ injection system. *International Journal of Greenhouse Gas Control* 37, 213-219, doi:10.1016/j.ijggc.2015.02.022.
- Siirila, E.R., Navarre-Sitchler, A.K., Maxwell, R.M., McCray, J.E., 2012. A quantitative methodology to assess the risks to human health from CO₂ leakage into groundwater. *Adv. Water Resour.* 36, 146-164, doi:10.1016/j.advwatres.2010.11.005.
- Singer, B.S., Dungan, M.A., Layne, G.D. 1995. Textures and Sr, Ba, Mg, Fe, K, and Ti compositional profiles in volcanic plagioclase: Clues to the dynamics of calc-alkaline magma chambers. *Am. Mineral.* 80, 776-798.
- Snæbjörnsdóttir, S.Ó., Wiese, F., Fridriksson, T., Ármannsson, H., Einarsson, G.M., Gislason, S.R., 2014. CO₂ storage potential of basaltic rocks in Iceland and the oceanic ridges. *Energy Procedia* 63, 4585-4600, doi:10.1016/j.egypro.2014.11.491.
- Stannius, L.S., 1998. Hydrothermal alteration, zeolite formation, and oil impregnation of basalts in the Marraat area, Nuussuaq, West Greenland. M.Sc. Thesis, University of Copenhagen, Copenhagen, Denmark.
- Stefánsson, A., Bénézech, P., Schott, J., 2013. Carbonic acid ionization and the stability of sodium bicarbonate and carbonate ion pairs to 200 °C – A potentiometric and spectrophotometric study. *Geochim. Cosmochim. Acta* 120, 600-611, doi:10.1016/j.gca.2013.04.023.
- Stefánsson, A., Bénézech, P., Schott, J., 2014. Potentiometric and spectrophotometric study of the stability of magnesium carbonate and bicarbonate ion pairs to 150 °C and aqueous inorganic carbon speciation and magnesite solubility. *Geochim. Cosmochim. Acta* 138, 21-31, doi:10.1016/j.gca.2014.04.008.
- Sverjensky, D.A., Shock, E.L., Helgeson, H.C., 1997. Prediction of the thermodynamic properties of aqueous metal complexes to 1000°C and 5 kb. *Geochim. Cosmochim. Acta* 61 (7), 1359-1412.
- Tutolo, B.M., Kong, X.-Z., Seyfried, Jr., W.E., Saar, M.O., 2014. Internal consistency in aqueous geochemical data revisited: Applications to the aluminum system. *Geochim. Cosmochim. Acta* 133, 216-234. doi.org/10.1016/j.gca.2014.02.036.

- Tutolo, B.M., Luhmann, A.J., Kong, X.-Z., Saar, M.O., Seyfried, Jr., W.E., 2014. Experimental observation of permeability changes in dolomite at CO₂ sequestration conditions. *Environ. Sci. Technol.* 48 (4), 2445-2452, doi:10.1021/es4036946.
- Tutolo, B.M., Luhmann, A.J., Kong, X.-Z., Saar, M.O., Seyfried, Jr., W.E., 2015. CO₂ sequestration in feldspar-rich sandstone: Coupled evolution of fluid chemistry, mineral reaction rates, and hydrogeochemical properties. *Geochim. Cosmochim. Acta* 160, 132-154, doi:10.1016/j.gca.2015.04.002.
- USEPA., 2012. 2012 Edition of the Drinking Water Standards and Health Advisories. Office of Water, U.S. Environmental Protection Agency, Washington, DC. EPA 822-S-12-001.
- Watson, M.N., Zwingmann, N., Lemon, N.M., 2004. The Ladbroke Grove–Katnook carbon dioxide natural laboratory: A recent CO₂ accumulation in a lithic sandstone reservoir. *Energy* 29 (9-10), 1457-1466, doi:10.1016/j.energy.2004.03.079.
- Weisenberger, T., Selbekk, R.S., 2009. Multi-stage zeolite facies mineralization in the Hvalfjörður area, Iceland. *Int. J. Earth Sci.* 98 (5), 985-999, doi:10.1007/s00531-007-0296-6.
- Wigley, M., Kampman, N., Chapman, H.J., Dubacq, B., Bickle, M.J., 2013. In situ redeposition of trace metals mobilized by CO₂-charged brines. *Geochem. Geophys. Geosy.* 14 (5), 1321-1332. doi:10.1002/ggge.20104.
- Wogelius, R.A., Walther, J.V., 1991. Olivine dissolution at 25°C: Effects of pH, CO₂, and organic acids. *Geochim. Cosmochim. Acta* 55 (4), 943-954.
- Wogelius, R.A., Walther, J.V., 1992. Olivine dissolution kinetics at near-surface conditions. *Chem. Geol.* 97 (1): 101-112, doi:10.1016/0009-2541(92)90138-U.
- Wunsch, A., Navarre-Sitchler, A.K., Moore, J., Ricko, A., McCray, J.E., 2013. Metal release from dolomites at high partial-pressures of CO₂. *Appl. Geochem.* 38, 33-47. doi:10.1016/j.apgeochem.2013.08.005.
- Wunsch, A., Navarre-Sitchler, A.K., Moore, J., McCray, J.E., 2014. Metal release from limestones at high partial-pressures of CO₂. *Chem. Geol.* 363, 40-55, doi:10.1016/j.chemgeo.2013.10.036.
- Xu, T., Apps, J.A., Pruess, K., 2004. Numerical simulation of CO₂ disposal by mineral trapping in deep aquifers. *Appl. Geochem.* 19 (6), 917-936.